Open Ceramics 3 (2020) 100008

Contents lists available at ScienceDirect

Open Ceramics

journal homepage: www.editorialmanager.com/oceram

Sintering of ceramics for clay in situ resource utilization on Mars

David Karl [a,*], Franz Kamutzki [a], Pedro Lima [b], Albert Gili [a], Thomas Duminy [a], Andrea Zocca [b], Jens Günster [b], Aleksander Gurlo [a]

[a] Fachgebiet Keramische Werkstoffe / Chair of Advanced Ceramic Materials, Institut für Werkstoffwissenschaften und -technologien, Technische Universitaet Berlin, Germany

[b] Bundesanstalt für Materialforschung und Prüfung (BAM), Berlin, Germany

ARTICLE INFO

Keywords:
Mars smectite
Clay ISRU
MGS-1 regolith simulant
Slurry additive manufacturing
Wet processing
Sintering
Simulated Mars atmosphere
In situ XRD
Martian pottery
Mars ceramics
Space pottery
Water absorption
Weibull analysis

ABSTRACT

The sintering of wet processed Mars global simulant green bodies is explored. Green bodies shaped using slip casting, throwing on a potter's wheel and additive manufacturing, including material extrusion (robocasting) and layerwise slurry deposition (LSD) are sintered in terrestrial and simulated Mars atmosphere. A sintering schedule is developed using hot stage microscopy, water absorption, sintering shrinkage and sintering mass loss. Sintered parts are characterized in respect to their density, porosity, phase composition, microstructure and mechanical properties. Densification behavior for different green bodies was generally similar, enabling the fabrication of larger green bodies (tiles, cups, bowls) and parts with fines details (test cubes and cuneiform tables) with low water absorption. Sintered LSD discs had a bending strength between terracotta and typical porcelains with 57.5/53.3 MPa in terrestrial/simulated Mars atmosphere. Clay ISRU for sintered ceramics can be considered an eminently favorable construction technology for soft and hard ISRU on Mars.

1. Introduction

Due to the vast distance from Earth, a continued human presence on Mars will only be feasible using local Martian resources - a practice labeled as in situ resource utilization (ISRU). Major consumables needed for a Martian settlement are energy, water, oxygen, food and construction materials [1]. Construction materials for habitat and equipment building are an early concern, due to the harsh climate, atmosphere and radiation conditions. In comparison to materials used in human civilization history on Earth, the absence of organic materials from plants is a significant challenge as the only available solid construction feedstock for early ISRU will be regolith and rocks. However, Mars is a differentiated terrestrial planet with complex geology and compared with the Earth's Moon, has a great variety of minerals, for example, felsic rocks [2], which in the presence of water can turn into phyllosilicates (clay minerals). Indeed, various clay resources are abundant on the surface of Mars [3] and up to this day, three distinct Martian regolith simulants have been introduced, which take smectite deposits into account [4]. In previous work, the authors have proposed that such clay deposits are of extraordinary value for ISRU efforts on Mars as the shaping of clay minerals into green bodies (one of the earliest human inventions originating before the Neolithic period) is a universal and versatile tool employed by all human civilizations [5].

In the same publication, the feasibility of a wet processing approach for Mars global simulants (MGS-1, introduced by Cannon *et al.* [6]) was shown - a versatile slurry system was introduced, which was further processed using four different wet-shaping methods producing green bodies with at least twice the green strength of dry pressed samples [5].

What is more, after shaping, such dried green bodies have high application flexibility, as illustrated by an example from the Roman empire, whose famous engineers used fired bricks in the harsh climates in Northern Europe while at the same time employing unfired bricks in the dry climates of Rome [7].

A similar bilateral approach is a promising clay ISRU scenario for Mars, as all that is required to wet process clay regolith into unsintered green bodies is a phyllosilicate resource, a temper mineral and water. If necessary, the clay green bodies can be further processed into high-density bricks or complex-shaped Martian pottery by sintering at high temperatures, which would only require an additional energy source.

* Corresponding author.
E-mail address: david.karl@ceramics.tu-berlin.de (D. Karl).

https://doi.org/10.1016/j.oceram.2020.100008
Received 28 May 2020; Received in revised form 8 June 2020; Accepted 22 June 2020
Available online 27 June 2020

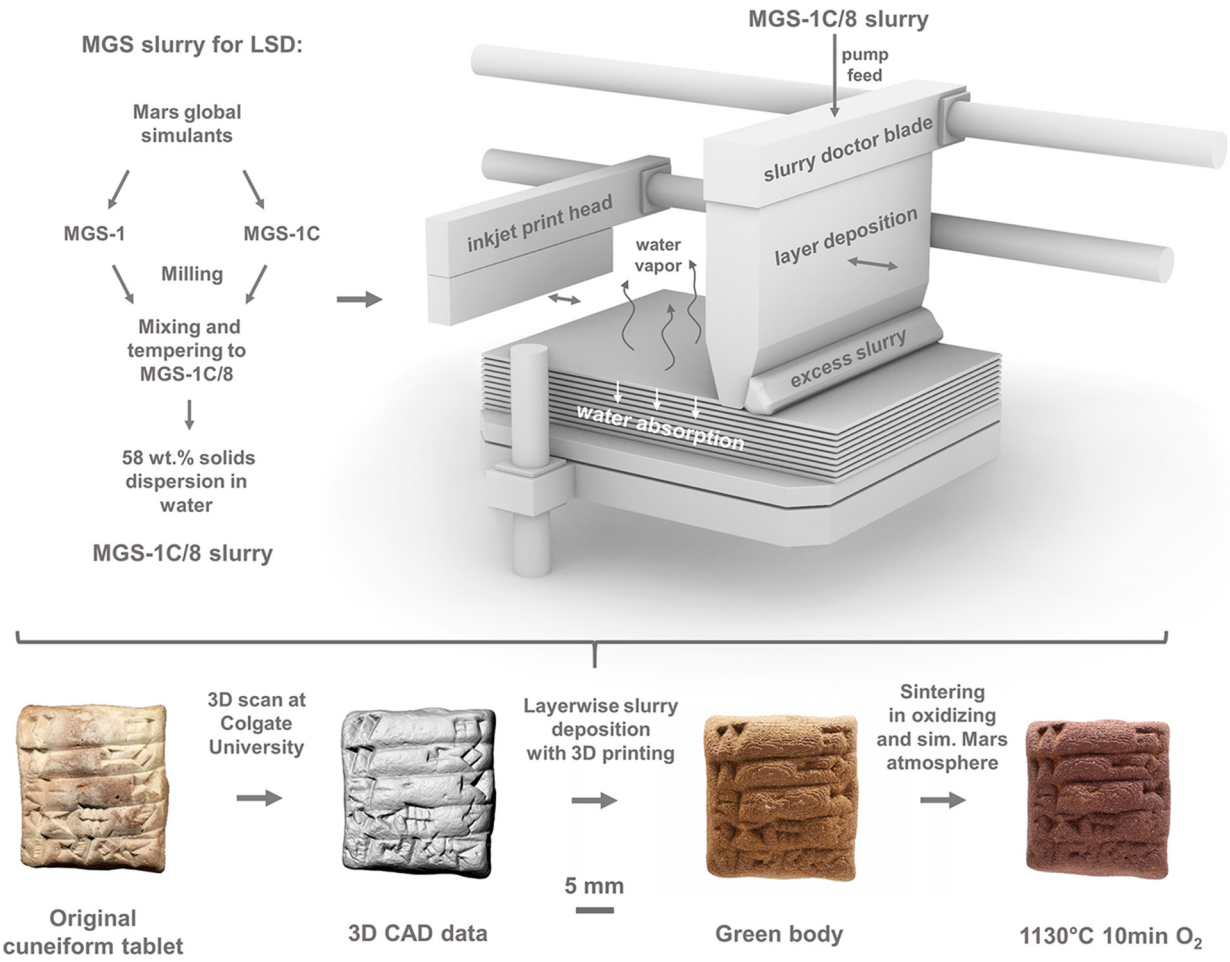

Fig. 1. (Top left) Flowchart of MGS slurry production (described in detail in Ref. [5]), (top right) schematic of the layerwise slurry deposition and (bottom) processing path for cuneiform tablets from 3D scans of original cuneiform tablets made during the Ur III period (ca. 2100-2000 BC), produced as technological demonstrators for LSD and inspirational artifacts for Mars colonization (image of original and CAD data with kind permission of Colgate University Libraries).

1.1. Additive manufacturing for ISRU

While half of the shaping procedures used in this work, slip casting and throwing on a potter's wheel, have a long tradition in ceramics manufacturing, the other two, material extrusion (robocasting) and binder jetting (powder bed 3D printing), fall into the category of additive manufacturing (AM). AM has received much attention for construction ISRU recently, as it would enable flexible remote production without astronauts being present. While many studies have proposed different AM concepts for ISRU on Mars [8–12], three studies have shown AM processing of Martian regolith simulants. First, laser fusion of pure regolith powder beds (powder bed fusion) produced constructs with a porosity $>$ 59% (no mechanical properties reported) [13]. Second, material extrusion of expensive biopolymer dissolved in toxic dichloromethane filled with regolith, produced elastic parts [14] and last material extrusion with phosphoric acid (of which at least 33 wt% would have to be shipped) gave parts with decent compressive strength [15].

Here, the sintering of green bodies shaped using the four wet processing methods (and one reference dry pressed) in Earth-like atmospheric conditions and various Mars-like atmospheric conditions is described. One aim was a sintering schedule for dense parts with $<$ 3 wt % absolute water absorption, which is typically the value to consider sintered ceramics frost-resistant [16]. The study of the sintering behavior in the current work was focused on samples produced by layerwise slurry deposition (LSD), as this was the most advanced and sophisticated processing method of the four considered here. The basic principle of LSD deposition coupled with binder jet 3D printing is depicted in Fig. 1.

To highlight the importance of clay as a medium for human civilizations and thought (along with illustrating the usefulness of the unfired/fired concept, as cuneiform tablets are found in unfired as well as fired state), cuneiform tablets from 3D scans we reproduced as inspirational artifacts, illustrating the excellent LSD printing resolution.

LSD is a novel AM technology that differs conceptually from dry powder bed AM technologies such as powder bed fusion (e.g., selective laser sintering/melting) and binder jetting (e.g., binder jet 3D printing) in that it uses a slurry/slip feedstock which is deposited via a doctor blade in 25–100 μm thick layers on a substrate and dried. Already during the deposition process, water is drawn into previous layers (by capillary forces), which act as a porous mold, creating a high-density powder bed with similar properties to slip cast green bodies that can reach a theoretical packing density of 55–70% [17]. Until now, two working principles to create 3D parts by fusing crosssections of each deposited layer have been developed, one in which laser energy is used to fuse the high-density powder beds [18] and another in which a binder fluid is ejecting through an inkjet print head [17,19]. For both approaches, post-processing is done by washing away the high-density powder bed, which leaves a water-resistant green body that might be used directly [5] but is typically post-processed by sintering in a furnace. LSD coupled inkjet printing is promising, as it produces ceramic parts with similar

mechanical properties to traditionally produced parts by slip casting or (isostatic-)pressing [17,19,20].

1.2. Sintering of green bodies in simulated Mars atmosphere

The sintering behavior under local atmospheric conditions is essential for various ISRU scenarios. The authors are only aware of Moon sintering studies, which have compared sintering of lunar regolith simulants in Earth-like atmosphere with different simulated Moon atmospheres - in vacuum [21,22], in hydrogen [23] and in argon [24].

For sintering in simulated Mars atmosphere (which is comprised of 94.9% CO_2 [25]), the authors envision a scenario in which minerals from Rocknest (MGS-1 mineralogy is based on Curiosity's first scoop [6]) would be sintered in Martian atmosphere in close vicinity to the excavation point. However, Mars atmospheric pressure changes significantly over the year, as the southern pole receives more sunlight and carbon dioxide is vaporized. Due to this effect, the atmospheric pressure changes during one Mars year by about 30%. Data from Curiosity's REMS instrument during the first scoop (made shortly after the autumnal equinox ($L_s = 180°$) at $L_s = 184°$ corresponding to Mars Science Laboratory (MSL) sol 61 [26]), showed a pressure of 772 Pa [27]. For sintering experiments in a tube furnace, with the aim to simulate the highest impact of CO_2 pressure on sintering, the authors choose 925 Pa CO_2 pressure for Mars sinter experiments. This would be equivalent to Curiosity's REMS measurements at the Glenelg Intrigue (400 m from its landing site) 109 sols later at 252°/MSL sol 170, briefly before the winter solstice ($L_s = 270°$) [27], that had the highest atmospheric pressure of all REMS measurements in Curiosity's first Martian year. Furthermore, sintering in a vacuum was examined, as vacuum conditions could easily be reproduced on Mars (due to the low overall pressure). For in situ XRD sintering experiments, the slightly lower CO_2 pressure of 610 Pa was simulated (which is the global mean annual surface pressure on Mars [28]), using a gas stream of N_2 mixed with CO_2 at 610 Pa partial pressure.

The principal goal of this work is to study the sintering of ceramics from clay ISRU green bodies made of tempered MGS-1C simulant (shaping experiments using a slurry wet processing approach to produce the green bodies were discussed in a previous publication [5]). Focusing mainly on parts produced using LSD, thermal properties using TGA and HSM are reported. Extensive sintering studies in ambient air and different simulated Mars atmospheres are undertaken (with sintering shrinkage, weight loss, water absorption and sintering color). Phase analysis ex situ and in situ, the microstructure of sintered parts and mechanical properties using Weibull analysis are described. A comparison with other standard non-technical ceramics and Martian ISRU ceramics finalizes the work.

2. Materials and methods

2.1. Materials

Two Mars regolith simulants developed by Cannon *et al.* (2019) - MGS-1 [29] and MGS-1C (a clay-modified version of MGS-1) [30] - were obtained from Exolith Lab (CLASS/UCF, Orlando, USA). MGS-1 is an open standard developed according to results from the X-ray diffraction measurements from the Mars Science Laboratory (MSL) rover Curiosity at the Rocknest aeolian bedform material - representative of the global basalt soil at Gale Crater on Mars [31]. According to the Exolith Lab data sheet [29], the phase composition of MGS-1 is (all wt%): plagioclase (27.1), basaltic glass (22.9), pyroxene (20.3), olivine (13.7), Mg-sulfate (4.0), ferrihydrite (3.5), hydrated silica (3.0), magnetite (1.9), anhydride (1.7), Fe-carbonate (1.4), hematite (0.5). The clay-modified MGS-1C is produced by mixing 40 wt% smectite clay (sodium montmorillonite) with the standard MGS-1 simulant. The amount of smectite in MGS-1C is based on the reference case of hydrated clay from a NASA Mars water in situ resource utilization study [32] and supported by MSL data which indicates a clay abundance at Gale crater from ~3 to 28 wt% (mostly smectite) [33]. Our previous publication showed that the essential properties of this smectite are similar or identical to the Wyoming MX-80 bentonite [5]. The final raw material for the slurries was a mixture of MGS-1 and MGS-1C, which is referred to here as MGS-1C/8.

2.2. Slurry preparation

2.2.1. Dry milling and tempering

MGS-1 and MGS-1C simulants (as delivered) were milled separately with a steel milling vessel in a TS250 vibrating disc mill (Siebtechnik GmbH, Germany). For each cycle, 200 g of powder was milled in four 2-min increments with 2-min cooling breaks to prevent changes in powder properties due to heat evolution. The ground powders were passed through a 250 μm sieve to break up clay agglomerates, which supports prompt dispersion. A new simulant composition with 5 wt% montmorillonite (MGS-1C/8) was produced from these milled powders by tempering 12.5 wt% MGS-1C (i.e., 1/8 - hence MGS-1C/8) with 87.5 wt % MGS-1.

2.2.2. Dispersion

Aqueous slurries with 58 wt% MGS-1C/8 solids load were prepared. An extensive dispersion study to fine-tune slurry rheology for LSD deposition was conducted earlier [5] and the electrosteric sodium polyelectrolyte dispersant Dolapix PC67 (kindly supplied by Zschimmer-Schwarz GmbH, Germany) was chosen in the ratio m(solid components of the slurry):m(-Dolapix PC67) = 200:1 (which corresponds to 0.5 wt% in relation to solid components of the slurry). To mix the slurry, the MGS-1C/8 powder was slowly poured into the water-dispersant mixture, which was vigorously stirred from above with an impeller stirrer, until all the powder was wetted. The resulting slurry was aged for 24 h and homogenized for 10 min on a roller bank before use (without milling balls).

2.3. Shaping technologies

2.3.1. Slip casting

For the slip cast samples, a conical cup mold made of casting plaster was generously filled with MGS-1C/8 slurry with 6 min casting time to produce thick-walled samples. The mold was emptied to remove the excess slurry and subsequently rotated for 120 s to create a smooth inner wall. After 24 h, the casts had detached and small casting defects were retouched using fresh slurry applied with a brush. After the green bodies had dried, retouched areas were sanded with 1000 grain sandpaper.

2.3.2. Shaping on potter's wheel and robocasting

To produce plastic bodies for throwing and robocasting, the water content of the MGS-1C/8 slurry was reduced by pouring the slurry onto filter paper, which was placed on a flat gypsum plate and allowed to stand until the solids/water content was 80 wt% MGS-1C/8 solids loading for throwing on a wheel and 75 wt% for robocasting. To throw a simple bowl, a circular polishing plate (Prätech Berlin GmbH, Germany) was used as a potter's wheel at 25–50 rpm. For robocasting, an Ultimaker 2 go (Ultimaker BV, Netherlands) was converted using a simple air-pressure controlled syringe-style cartridge and a 0.84 mm diameter dispensing needle (both Vieweg GmbH, Germany) for extruding the MGS ceramic mass (75 wt% solid loading) at pressures of 3–4 bar.

2.3.3. Layerwise slurry deposition coupled with 3D printing

A custom build LSD system described previously [17], was used to deposit layers of MGS-1C/8 slurry. After each layer was dried, an inkjet printhead was used to infiltrate specific regions (the single slices of 3D objects) using a proprietary resin binder. This process was repeated until the whole part was built. For the LSD system, axes are defined with X being the direction parallel to the movement of the doctor blade, Y perpendicular to X in the plane of a layer and Z the axis in which layers are stacked (perpendicular to the layer plane). First, disc-shaped samples

with diameter 16 mm and height 2.5 mm were printed flat in the XY plane for biaxial mechanical strength evaluation by the ball on three balls method, which is well suited for as-sintered samples [34]. Second, cubic samples with 12/8/10 mm in X/Y/Z-direction for sinter shrinkage analysis were built (as LSD prints shrink slightly more in Z-direction, which is typical for powder bed processes - an issue that can be corrected in the 3D model stage [17,19]). Third, to highlight the importance of clay for early civilizations and to give an impression of LSD print resolution, reproduction of Sumerian cuneiform tablets from the Ur III period (ca. 2100-2000 BC) were LSD printed (see Fig. 1). The Hub at Colgate University kindly provided STL files from 3D scans of the tablets held in the collection of Colgate University Libraries at Hamilton, New York (USA) and described in detail by Snell and Lager [35]. After printing, the LSD printed blocks with the substrate were taken out of the machine and post-cured at 100 °C for 12 h. Subsequently, printed green bodies were removed from the high-density powder bed by carefully washing with deionized water, followed by drying in air for at least one week.

2.3.4. Dry pressing

Square MGS-1C tiles ($6 \times 6 \times 1$ cm^3) were produced by dry pressing MGS-1C/8. For this, a stainless steel dye was filled with 80 g of milled (but not pre-dried) MGS-1C/8 (without dispersant) and pressed at 70 MPa for 3 min using an electrohydraulic press (Paul -Otto Weber GmbH, Germany).

2.4. Sintering

2.4.1. Sintering under oxidizing conditions

Aiming at a sintering schedule for dense parts with little sintering/pyroplastic deformation, an extensive sintering study was undertaken using a K1252 oven (Heraeus GmbH, Germany) with open heating elements. All samples were sintered in air at a heating rate of 1.7 K/min. For each schedule, a minimum of three samples was placed at the edges of the sintering area (to investigate deviations from different oven zones). Sintering temperatures ranged from 1000 °C with 10 min–1160 °C with 10 h dwell time followed in one step and two-step ramps and all schedules were followed by furnace cooling at 1.7 K/min and placing samples in a desiccator. The final ramp selected to sinter discs for mechanical tests, was a two-step ramp with the first step at 1150 °C for 3 h dwell time and the second step at 1160 °C for 90 min dwell time followed by cooling (all heating and cooling at 1.7 K/min).

2.4.2. Sintering under simulated Mars conditions

Three different sintering atmospheres relevant for ISRU on Mars were studied: (i) vacuum, (ii) 925 Pa CO_2 with non-pre-sintered green bodies and (iii) 925 Pa CO_2 with green bodies pre-sintered at 1000 °C in oxidizing atmosphere. A custom build Al_2O_3 tube furnace inside an HT 1600 (LECO Instrumente GmbH, Germany) was used to heat samples from room temperature to the maximum temperature between 1130 °C and 1160 °C with 10 min to 10 h dwell time at 1.7K/min heating/cooling rate for all three atmospheres. For (i) vacuum, samples were placed inside the sealed tube furnace, which was being continuously evacuated (for the duration of the whole ramp) up to $\sim 2 \times 10^{-3}$ mbar by a rotary vane vacuum pump RV8 (Edwards Limited, UK). To simulate Martian atmosphere more closely, samples in different states, with (ii) non-pre-sintered green bodies, and (iii) pre-sintered at 1000 °C (in the oxidizing atmosphere described above), were sealed in the tube furnace which was evacuated (10 min) and flushed with CO_2 three times before being filled with CO_2 at a pressure of 925 Pa (see the introduction for details) and sealed at 20 °C followed by sintering at the different temperatures. The final conditions selected to sinter for mechanical tests, was (iii) at 925 Pa CO_2 with pre-sintered discs using a two-step ramp with the first step at 1145 °C for 3 h dwell time and the second step at 1160 °C for 90 min dwell time followed by cooling (all heating and cooling at 1.7 K/min).

2.5. Characterization methods

Thermogravimetric (TG) and derivative thermogravimetry (DTG) characterization were performed in an STA409 PC/PG (Netzsch GmbH, Germany) using Al_2O_3 crucibles. Samples were air-dried and ground and subsequently heated in air from 25 to 1300 °C at a heating rate of 1.7 K/min. Side-view hot stage microscopy (Hesse Instruments, Germany) was performed on cylinders with a 3 mm width and height produced by grinding LSD green bodies and hand pressing with 1.5 N/mm^2 as described before [36]. Area shrinkage was measured in air with a heating rate of 2 K/min up to the respective temperature and holding for 10 h in a tube kiln. Due to equipment design, detailed thermal analysis (TG/DTG, HSM) could only be conducted for sintering in ambient air. Sintering shrinkage and sintering mass loss of three samples for each temperature were determined (and results averaged) by measuring the length and mass of green and sintered bodies before and after sintering using the digital Micromar micrometer (Mahr GmbH, Germany) and the laboratory balance Genius ME215P (Sartorius, Germany). Three different water absorption measurement procedures were used (repeating each measurement three times): Procedure A was a simplified method used to characterize samples between furnace runs directly. For this fast method, sintered bodies were taken directly from the furnace, weighed and fully immersed in deionized water. After 10 min, the individual samples were taken out and tapped dry once from each side with precision wipes and the mass was recorded. For selected samples, two further water absorption procedures were used to calculate a pore interconnectivity factor and evaluate frost-resistance: Procedure B was similar to the 10 min test A only with 120 °C for 24 h pre-drying and water absorption for 24 h. Procedure C was after normative ISO 10545-3:1995 [37] for which whole sintered samples were dried at 120 °C for 24 h and dry mass was recorded. Subsequently, the samples were immersed in boiling deionized water for 2 h after which the heating system was switched off and samples were left to cool naturally for 4 h still immersed in water for further saturation. Samples were taken out of the water using plyers and excess moisture was removed using a damp cloth (the cloth was carefully wetted with twice its weight of deionized water) before mass was re-recorded. Bulk density of samples selected for mechanical tests was determined using Archimedes' boiling method from ISO 18754:2013(E) [38]. To determine the amount of closed porosity, pycnometer density of whole discs was measured with a helium gas expansion multivolume pycnometer 1305 (Micromeritics Instrument Corp., USA) after thoroughly drying discs (105 °C for 24 h under vacuum) using five repetitions and averaging the results. Subsequently, discs were broken with a Plattner's mortar and pulverized by silicon carbide mortar. Finally, fine powders were dried (105 °C for 24 h under vacuum), after which true powder particle density was measured by pycnometer as described above for whole discs and porosity values calculated using equations described elsewhere [39]. XRD was measured in situ and ex situ. In situ synchrotron transmission X-ray powder diffraction (XRD) was performed at beamline 12.2.2 of the Advanced light source (ALS) at the Lawrence Berkeley National Laboratory (Berkeley, USA) with 25 keV radiation ($\lambda = 0.49594$ Å) in an oven setup described previously [40,41]. Powder samples were placed in 700 μm quartz capillary sample holders either in ambient air or in a simulated Mars atmosphere (a mixture of 33 Nml/min N_2 and 0.2 Nml/min CO_2 resulting in a CO_2 partial pressure of 610 Pa) and heated with 10 K/min to 1200 °C followed by natural cooling. During heating, XRD patterns were measured with an XRD 1621 image plate detector (PerkinElmer, USA). Ex situ XRD measurements were done using a Bragg-Brentano geometry D8 Advance diffractometer (Bruker Corporation, USA) with Co-Kα radiation ($\lambda = 1.7902$ Å) and a SOL-X detector. Optical micrographs of sintered discs embedded in epoxy resin using a vacuum chamber and subsequently polished were taken using the digital microscope DM4000 M (Leica, Germany). Ball on three balls setup was used to test the biaxial mechanical strength of LSD printed discs. Two final sintering schedules were chosen, one in oxidizing atmosphere and one in (iii) simulated Mars atmosphere both focusing on small sintering

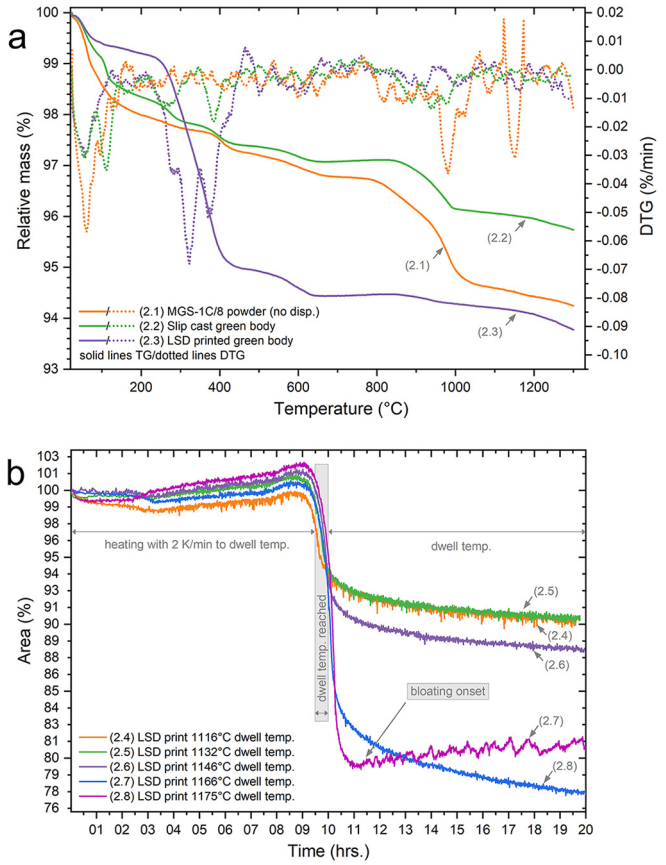

Fig. 2. (a) Thermogravimetric analysis of (2.1) MGS-1C/8 raw powder, (2.2) dried MGS-1C/8 slurry with 0.5% dispersant and (2.3) LSD printed parts with dispersant and binder before sintering. (b) Hot stage microscopy (HSM) analysis of LSD printed samples at temperatures from 1116 °C to 1175 °C with 10 h dwell time each.

deformation, a wide processability window and relative dense sintering. For each sintering schedule, 30 samples (all XY-plane) of the above described sintered LSD discs were broken with stainless steel balls (diameter 7 mm) on a Z005 testing machine (Zwick Roell, Germany) with 5 kN load cell at a deformation speed of 10 μm/s. CES Selector 2019 software (Granta Design, UK) was used to draw graphs comparing water absorption of terrestrial ceramics and evaluating various ISRU material concepts.

3. Results and discussion

3.1. Choice of sintering conditions

3.1.1. Pre-sintering characterization of thermal behavior

TG curves in ambient air of (2.1) raw MGS-1C/8 powder, (2.2) a slip cast green body (made from MGS-1C/8 slurry with dispersant) and (2.3) LSD printed green parts (containing both dispersant and binder) show a respective mass loss of (2.1) 5.75%, (2.2) 4.26% and (2.3) 6.22% at 1300 °C (Fig. 2a).

(2.1) and (2.2) TG profiles show similar behavior with the surprising result for the slip cast green body (with dispersant, 85% weight loss on ignition for dispersant given by manufacturer) of 1.49% less mass loss in comparison to the starting raw powder (without dispersant). This discrepancy can be explained by the migration of 4 wt% epsomite/magnesium sulfate ($MgSO_4{\cdot}7H_2O$) component in MGS-1 into the gypsum mold during casting, which created efflorescence (a concentration gradient) in the slip cast parts that showed a darker inside when dry. After sintering, these darker parts gave a light-yellow stain, which is consistent with a phenomenon called scumming (described further in 3.1.4). Similar scumming was observed for robocast parts and LSD powder beds where the regions to dry last (corners) were slightly darker - however, the final LSD parts did not show darker regions (as the powder bed was printed in the center). With 94.96% mass loss at 1000 °C for MGS-1C/8, our measurement compares well to 96.4% mass for nonclay MGS-1 found by Cannon *et al.* at the same temperature [2]. We attribute the 1.44% extra mass loss to different amounts of H_2O in the simulants

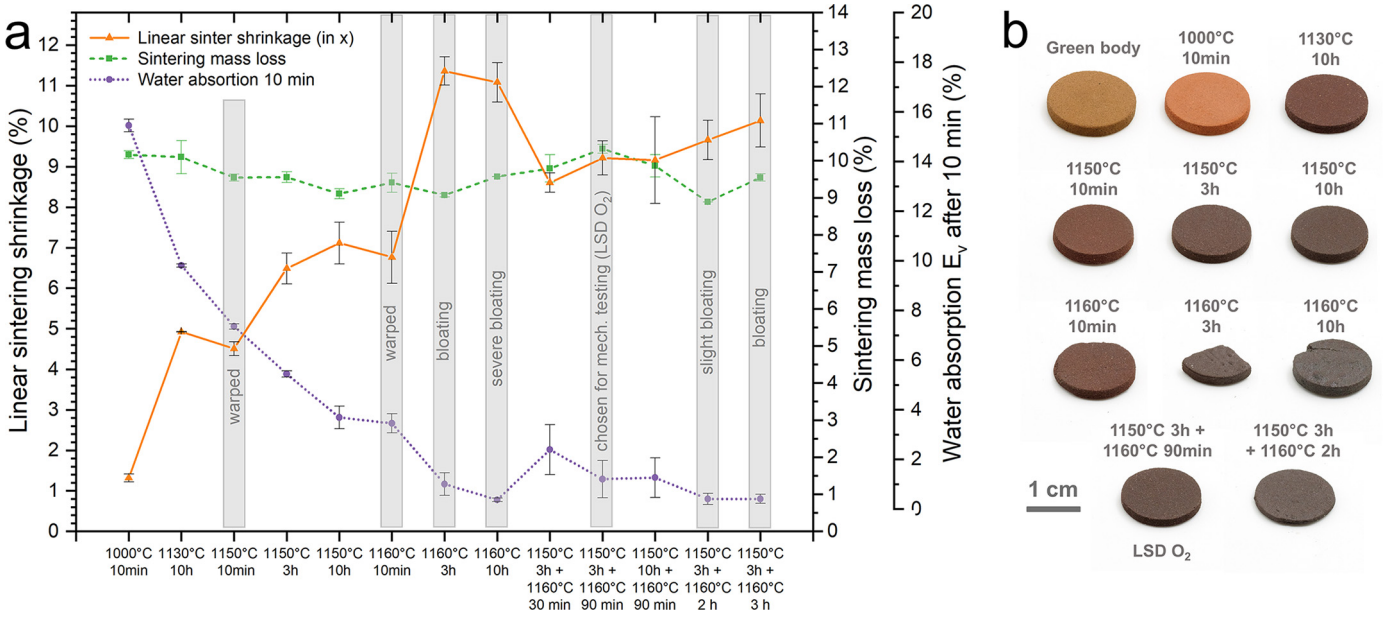

Fig. 3. (a) Sintering conditions in oxidizing atmosphere and (b) images of selected sintered samples. Geometrical and thickness variations, as well as cracks, were already present in the green bodies before sintering. (For interpretation of the references to color in this figure legend, the reader is referred to the Web version of this article.)

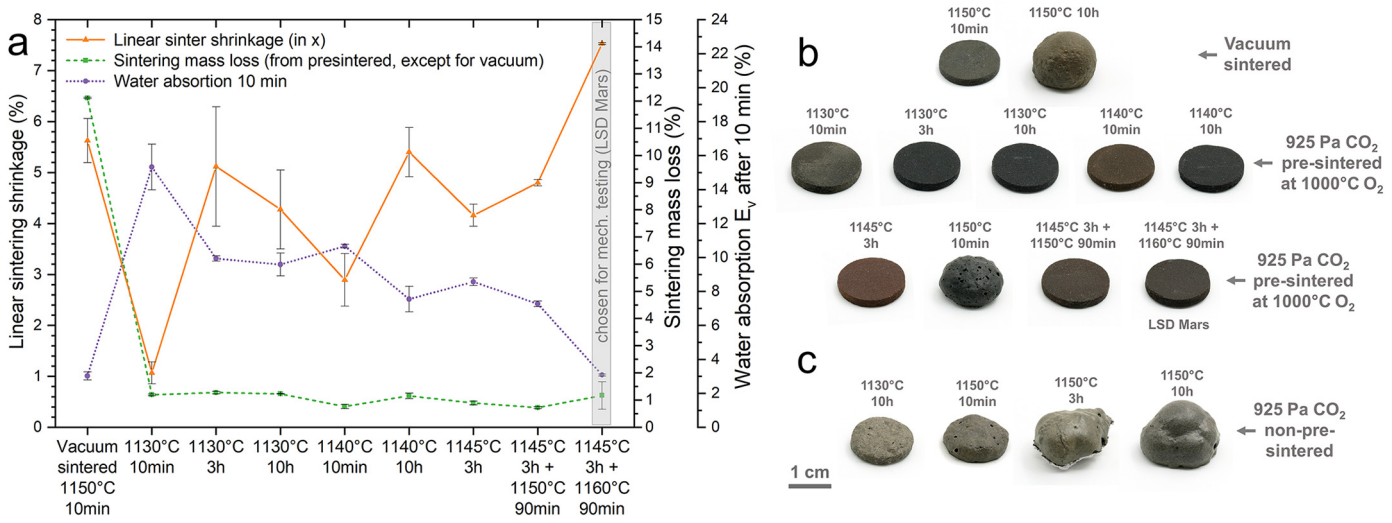

Fig. 4. (a) Sintering conditions in simulated Martian conditions. (b) Images of selected sintered samples (bloated samples not depicted in (a)). (c) Images of samples sintered without pre-sintering leading to bloating (samples not depicted in (a)).

due to storage in ambient air, as well as additional H_2O retained by the 5% smectite component, which is hygroscopic. In detail both (2.1) and (2.2) show a continuous mass loss starting from 20 °C due to the release of H_2O, the decomposition of the dispersant (only for (2.2)) and the breakdown of the 1.4% Fe-carbonate/siderite MGS-1 content releasing CO_2 [42], here until ~ 625 °C where both (2.1) and (2.2) reach a plateau. The further sharp mass loss starting at ~825–850 °C and slowing down at 1000 °C for (2.1) and (2.2) can be attributed to SO_2/SO_3 and O_2 release [6] due to the thermal breakdown of the 4 wt% epsomite (that is in the anhydrous Mg-sulfate state at this temperature) to MgO and SO_3 (which in turn breaks down to SO_2 and O_2). The TG profile of the LSD printed sample (2.3) differs as there is a steep mass loss between 300 and 400 °C, which is related to a decomposition of the polymeric binder. Furthermore, the Mg-sulfate decomposition for (2.3) is less pronounced, which would suggest that the washing of the sample during powder bed removal resulted in the removal of the salt. At 1200 °C DTA curves (data not depicted) for (2.1), (2.2) and (2.3) show peaks that can be attributed to the melting of the samples, which fits well with our HSM and sintering study results in the next paragraph.

A hot stage microscopy study in ambient air (Fig. 2b) revealed that pressed tables from ground LSD printed parts (2.4–2.8) would continuously shrink over 10 h when sintered up to 1166 °C. However, the sample sintered at 1175 °C for 10 h (2.8) showed severe bloating starting after around 1 h dwell time, which is a sudden onset of bloating and constitutes a narrow sintering interval as at 1166 °C no area increase was registered at all. Bloating occurs when bodies mature at higher temperatures leading to closed pores, which in turn prevents gases from leaving the body. Not all clay containing bodies bloat when overfired (some lose their shape by melting), as bloating depends on the ratio and composition of fluxing and gas-forming agents in a body [43], as well as their grain size and distribution. Gases to cause bloating (individually or in combination) are oxygen from the reduction of hematite (Fe_2O_3) to magnetite (Fe_3O_4), carbon dioxide/monoxide released by carbonates, sulfur di/trioxide released by gypsum, water from clay minerals and the oxidation of iron sulfide minerals [44]. Here, compounds (in LSD printed parts) releasing gas during sintering are hematite, ferrihydrite ($Fe^{3+}{}_{10}O_{14}(OH)_2$), Fe-carbonate ($FeCO_3$), anhydride ($Ca[SO_4]$), as well as epsomite - in sum, these constitute 9.1 wt% of the total MGS-1 - in addition to organics from dispersant/binder and water from montmorillonite.

3.1.2. *Sintering of LSD green bodies in oxidizing conditions*

Sintering of LSD green body discs in ambient (oxidizing) atmosphere produced stable ceramic parts that showed a linear sinter shrinkage from 1.3 to 11.4% (Fig. 3).

There is a clear inverse correlation between sintering shrinkage and water absorption (here 10 min/procedure A), as the schedule with the highest shrinkage produced samples with the lowest water absorption. This is what is to be expected from typical sintering densification as the body shrinks (without losing shape/melting) and the number of pores is reduced. A small deviation from this relationship can be seen in the 1160 °C 10h sample, which had the lowest water absorption but only the second-highest sinter shrinkage. The lower shrinkage value stems from the severe bloating of this sample as the surface defects reduced the measured value. Similarly, the shrinkage value of the 1150 °C 10min and 1160 °C 10min samples was influenced by the deformation of the sample due to warping and should have been slightly bigger. No clear trend for sintering mass loss was found, as all LSD samples were in a similar range from 8.89 to 10.32%. The authors expect deviations not to be related to the different sintering temperatures or bloating behavior but be the result of storing green bodies in ambient (not controlled) atmosphere before weighing and sintering them.

LSD discs matured rapidly with distinct changes in water absorption and sintering color related to changes in maximum temperature and sintering time. As indicated by HSM (Fig. 2b), over-firing lead to bloating of LSD parts with lens-shaped blisters in the inside and closed pores on the outside (such parts did absorb very little water). Samples with short dwell time (10 min) at 1150 °C or 1160 °C had a tendency for slight warping, which could be related to uneven heat distribution (in connection with high pyroplasticity at peak temperatures) for short dwell times. The best parts for single-step sintering were at 1150 °C for 10h, which had a linear shrinkage of 7.12 ± 0.51% and water absorption (after 10 min) of 3.69 ± 0.45%. Heating in a single step to the slightly higher temperature of 1160 °C led to bloating. Subsequently, two-step ramps were used, with first heating to 1150 °C and holding to release as much gas as possible (while pores are still open) and then increasing to 1160 °C to close pores. The best schedule for dense and reproducible parts with sufficient margin (no significant deviation on sintering in different locations in the furnace), was to heat to 1150 °C for 3h and then to 1160 °C for 90 min which gave parts with linear shrinkage of 9.14 ± 0.28% and water absorption (after 10 min) of 1.21 ± 0.75% that did not show visible bloating. Samples sintered at these conditions (1150 °C 3h + 1160 °C 90min, in oxidizing atmosphere) and used for mechanical tests are dubbed "LSD O_2" hereafter.

However, increasing holding time for this schedule by 30 min at 1160 °C (to 1150 °C 3h + 1160 °C 2h) lead to very mature bodies that were visibly vitrified as they had a glossy surface, did absorb very little

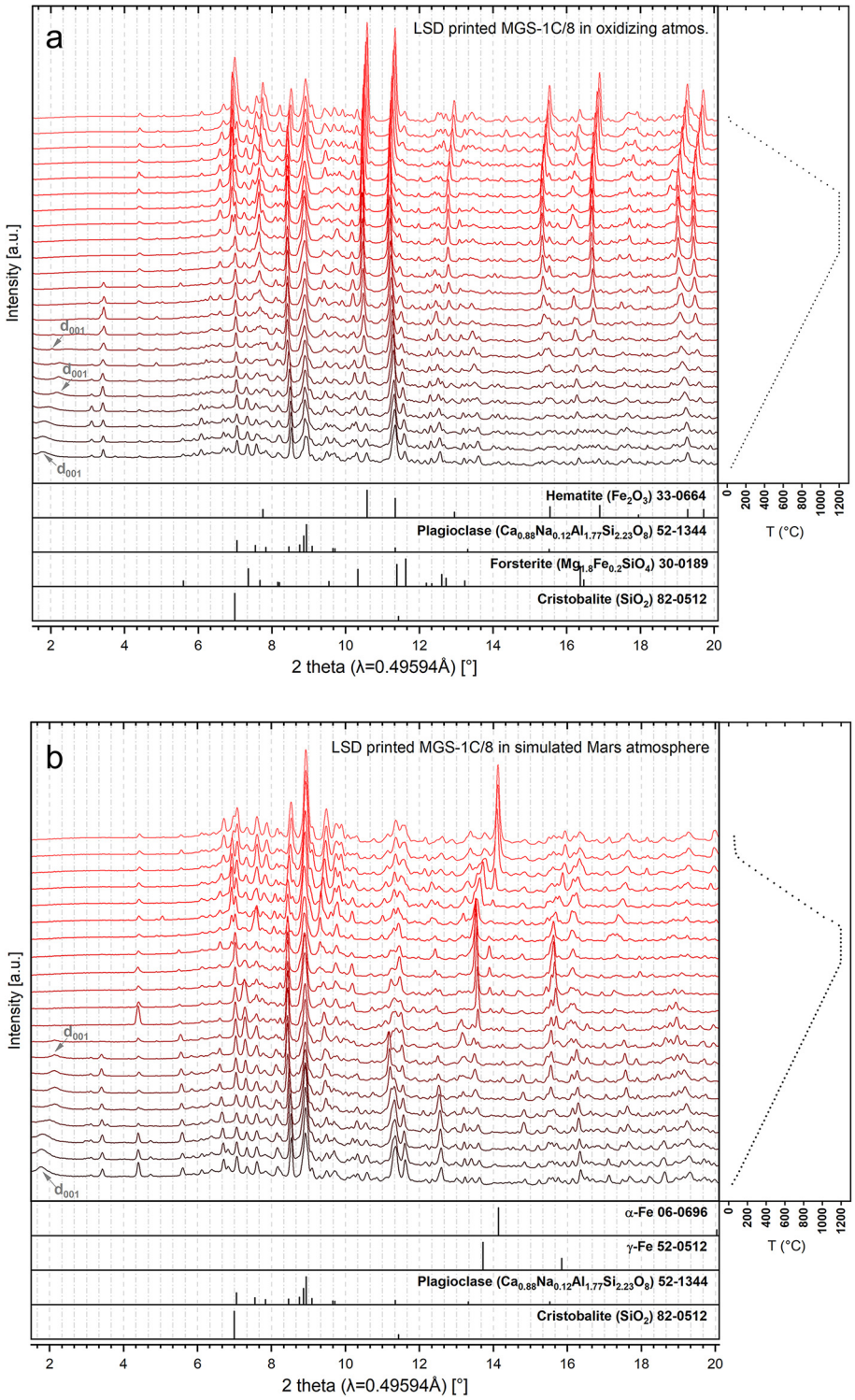

Fig. 5. Ceramics sintered from green bodies using the versatile MGS-1C/8 slurry system employing classic pottery (potter's wheel), slip casting, material extrusion (robocasting/direct ink writing), 3D printing (layerwise slurry deposition with binder jetting) and as a reference dry pressing. Green bodies are depicted in Fig. 6 in our previous work [5]. (For interpretation of the references to color in this figure legend, the reader is referred to the Web version of this article.)

water (0.41 ± 0.23%) and showed onset of bloating (Fig. 3b).

After sintering, a color change from brown to light red (1000 °C 10min) to dark red (1150 °C 10min) to dark purple (1160 °C 10h) was observed (Fig. 3b). A similar color pallet is typical for terracotta clays that are traditionally fired below 1100 °C and produce light red wares. However, firing such terracotta clay to high maturity at similar temperatures used here also produces purple wares. These distinct colors stem from the iron content in the materials, as iron is the dominant cause of coloration in pottery [45].

XRD indicates that the main crystalline iron phase in oxidizing atmosphere is hematite and precisely this color change from red to purple has been shown to occur in pure hematite pigment that was annealed in

the range from 500 to 1000 °C [46]. Various authors have suggested that the particle size of hematite is the primary source of this color shift, with increased particle size resulting in darker color [46–48]. Schwertmann and Cornell (their plate VI) depict this shift for ~0.1 μm hematite (red) to 0.4 μm hematite (purple) [48]. We expect similar effects in our specimens.

3.1.3. Sintering LSD green bodies in simulated Mars atmosphere

LSD printed tables were sintered in three different atmospheres relevant for ISRU on Mars (i) vacuum, (ii) 925 Pa CO_2 with non-pre-sintered green bodies and (iii) 925 Pa CO_2 with green bodies pre-sintered at 1000 °C in oxidizing atmosphere. Compared with sintering in oxidizing atmosphere, for all three simulated Mars atmospheres, LSD samples showed a tendency to suddenly bloat with extreme volume expansions, compared to a more gradual bloating in oxidizing atmospheres (Fig. 4b).

The tendency to bloat in reducing atmosphere is associated with the reduction of Fe_2O_3, to FeO by CO [49]. FeO is a powerful flux on silica, resulting in a glassy phase that closes pores in the vitreous body leading to bloating as other gases are trapped during their release [50]. Comparing LSD discs (Fig. 4b) sintered in (i) vacuum at 1150 °C 10 min (with binder and continuously applied vacuum pump) to discs sintered at 1150 °C 10 min and 925 Pa CO_2 in (ii) non-pre-sintered and (iii) pre-sintered condition, the latter two show extensive bloating. It is important to note, that continuously simulating CO_2 Mars atmosphere conditions during sintering proved challenging, as a closed environment (tube furnace) was used to keep CO_2 at 925 Pa for (ii) and (iii). Due to this sealed furnace, a release of gas from the samples resulted in a changed atmosphere in the furnace, which influenced sintering behavior. Pressure during sintering in the closed furnace increased for (ii) non-pre-sintered LSD samples and after cooling pressure was at 16–18 kPa. While several compounds in LSD printed samples release gases, contributing to a complex furnace atmosphere (as discussed in 3.3.1), LSD samples were pre-sintered at 1000 °C in oxidizing atmospheres, which reduced the pressure increase for (iii) after cooling to only 4–6 kPa. The authors attribute the extreme bloating behavior of (ii) to the presence of high amounts CO from the decomposition of LSD binder, as parts from other shaping technologies (that were non-pre-sintered) did sinter similarly (when the furnace was run without gas releasing LSD parts) to the pre-sintered LSD parts in (iii).

As shown previously, traces of carbon left inside wares at high temperatures can lead to bloating [51], which is what was observed for all non-pre-sintered samples (ii). The decomposition of the carbon-containing binder resulted in high CO concentrations, which made the sintering of such samples without bloating even at lower temperatures impossible (Fig. 4b). However, in real ISRU sintering on Mars, this problem could be mitigated by circulating a gas stream through the furnace, which could transport CO released from organic binders out of the furnace atmosphere.

Non-bloated samples sintered under (i) and (iii) conditions showed a linear sinter shrinkage (Fig. 4a) from 1.06 ± 0.21 to 7.53 ± 0.02%, which was lower than samples in oxidizing atmosphere and consequently produced bodies with a higher water absorption after 10 min of 12.32 ± 1.34 to 3.02 ± 0.23%. With the exception of the vacuum sample (with had a lower shrinkage), the ratio of shrinkage to water absorption between samples from oxidizing and simulated Mars atmosphere was somewhat similar (for example comparing discs sintered at 1150 °C for 10h in oxidizing atmosphere and at 1145 °C 3h + 1160 °C 90 min in CO_2). Mass loss was recorded from the pre-sintered condition and was from 0.72 ± 0.03 to 1.13 ± 0.04% (except for the vacuum sample which was recorded from non-pre-sintered samples with 12.11 ± 0.02%), while the averaged mass loss during pre-sintering to 1000 °C in oxidizing atmosphere was 9.18 ± 0.72%. No clear trend correlating mass loss with temperature was found and fluctuations are deemed to result from storage in ambient air, as discussed for air sintered samples. Sintering in vacuum at 1150 °C 10min lead to almost dense ceramics with the lowest water absorption after 10min of all samples sintered in simulated Mars atmosphere (3.02 ± 0.23%) and lower than for parts sintered at the same schedule in oxidizing atmosphere that had 7.36 ± 0.11%. Increasing sintering time to 10h in vacuum lead to extreme bloating with foamed sphere-shaped samples (Fig. 4b) that had very large interconnected pores in the inside. Concerning ISRU efforts, sintering in vacuum on Mars is less challenging than in oxidizing atmosphere, has lower resource requirements and is therefore deemed a viable alternative to sintering in real Mars atmosphere.

For pre-sintered discs in CO_2 (iii), the maximum sintering temperature for the first step was set to 1145 °C as heating to 1150 °C 10 min lead to a dark black glassy foam. Similar to the oxidizing atmosphere sintering, a two-step ramp was introduced and the sintering schedule was fixed to 1145 °C 3h + 1160 °C 90min for the production of parts for mechanical tests(to compare parts from air and CO_2 sintered at similar temperatures), which gave decent parts with 3.08 + 0.06% water absorption after 10 min. For the second step, no higher temperatures or longer holding times were explored, which might lead to further densification (before bloating sets in). Samples sintered under these conditions (1145 °C 3h + 1160 °C 90min, pre-sintered tablets in CO_2 (iii)) and used for mechanical tests are dubbed "LSD Mars" hereafter.

After sintering in the different simulated Mars atmospheres, colors were distinctly different from samples sintered in oxidizing atmosphere with a palette from grey to black (as well as three red-brown samples). The black color after sintering of iron-containing clays stems from the reduction of iron oxide phases by carbon monoxide, forming magnetite (Fe_3O_4) or wüstite (FeO), which are both black at all temperatures [51]. While samples sintered in vacuum (i) show dark grey color, bloated/-glassy samples from non-pre-sintered (ii) discs were light grey, similar to the grey color of ancient pottery (Grey Minyan) which was also sintered in reducing atmospheres (and showed the spinel group mineral hercynite [52]).

Pre-sintered samples (iii) had different shades of black (except for one red-brown and two darker red-brownish ones) associated with magnetite/wüstite. Samples with red-brown colors were taken out of the furnace at ~300 °C (due to long cooling times) into ambient air and the colors are a result of the reoxidation of magnetite into maghemite (γ-Fe_2O_3) [48], a typical problem at cooldown when aiming to produce black wares by flashing [51].

3.1.4. Sintering behavior of larger parts and comparison of different shaping methods

Comparing sintering behavior for all five different shaping methods, densification behavior and sintering color differed slightly between methods for the same sintering conditions (see Fig. 5).

While large demonstrator pieces could be sintered without cracking, volume and part geometry also played an essential role in sintering outcome - while the big and upward standing slip cast cup in Fig. 5 showed severe bloating, slip cast samples sintered with the same schedule (but lying flat on the sinterplate) showed no bloating. This is a result of choosing to sinter very mature bodies, which lead to the described small sintering interval before the set in of bloating. If relatively dense ceramics with low water absorption are to be sintered, the sintering schedule needs to be adjusted to part volume and geometry. Furthermore, while sintering of thrown, robocast and LSD printed samples showed generally similar color when sintered at 1130 °C for 10h in oxidizing atmosphere, the slip cast cup and dry pressed tile both sintered in the same furnace run (cup upright, tile flat) did not result in absolutely identical colors.

The sections of green parts (especially from robocasting and slip casting) to dry last had a darker surface from efflorescence (e.g., the right corner of robocast green body in Fig. 5). This was a result of the high magnesium sulfate solvability, as the salt migrated to regions that dried last, which were the corners of robocast parts and the inside of slip cast parts. After sintering these darker regions developed a white stain for 1000 °C in oxidizing atmosphere (corner robocast sample) and a yellow

Table 1
Properties of sintered samples from different shaping methods: dry pressed, slip cast, hand build, robocast, LSD O_2 and LSD Mars (see 3.1.2 and 3.1.3 for the LSD sintering conditions). All samples were sintered lying flat on the support plate. Data obtained from three samples for each property.

Shaping method	Green body porosity (%) [5]	Sinter shrinkage (%)	Sintering mass loss (%)	Water absorption 10 min (%)	Water absorption 24h A_l (%)	Forced water absorption ISO 10545-3 A_f (%)	Pore interconnectivity A_x (%)
Dry pressed[a]	31.83 ± 0.47	5.03 ± 0.28	6.28 ± 0.03	3.12 ± 0.94	4.61 ± 1.46	7.99 ± 1.19	42.30
Slip cast[a]	42.19 ± 0.64	9.14 ± 0.17	5.19 ± 0.09	1.33 ± 0.74	2.03 ± 1.10	5.87 ± 0.97	65.42
Hand build[a]	37.69 ± 0.52	4.06 ± 0.17	3.56 ± 0.01	3.89 ± 0.53	4.99 ± 0.50	9.54 ± 0.36	47.69
Robocast[a]	36.87 ± 1.09	9.30 ± 0.11	6.39 ± 0.04	0.65 ± 0.08	0.75 ± 0.11	2.83 ± 0.03	73.50
LSD O_2	38.26 ± 0.34	9.21 ± 0.42[b]	10.32 ± 0.12	1.21 ± 0.75	1.58 ± 0.98	5.50 ± 1.09	71.27
LSD Mars	38.26 ± 0.34	7.53 ± 0.02[b]	1.17 ± 0.51[c]	3.08 ± 0.06	3.33 ± 0.34	6.73 ± 0.54	50.52

[a] Sintered in oxidizing atmosphere at 1150 °C for 3h + 1160 °C for 90min (conditions identical to LSD O_2).
[b] Sinter shrinkage in X direction.
[c] Weight loss from pre-sintered state (1000 °C 10 min in oxidizing atmosphere).

stain when sintered above 1000 °C oxidizing atmosphere (corner robocast sample and spots on the rim of thrown cup) but not in simulated Martian atmosphere (robocast sample). Such stains are a common observation called scumming when clays with soluble salts are sintered. Scumming produces insoluble stains that are usually white but may be yellow or pink (with no evidence for stains to affected durability) [53]. During sintering, silica and magnesium sulfate react (magnesium sulfate decomposition temperature is lowered from 880 °C to 680 °C when silica is added to magnesium sulfate [54]), forming magnesium scum which is forsterite (Mg_2SiO_4) or enstatite ($Mg_2Si_2O_6$) [51].

Similar to the other sintering studies, shrinkage for samples from different shaping methods (Table 1) was related to water absorption, which was in the range of 0.65 ± 0.08 to 3.89 ± 0.53% after 10 min immersion.

Green body porosity did not seem to be the determining factor for sintered body water absorption, as the sample with the highest porosity (slip cast) did show water absorption (10min/procedure A) in the mid-range with 1.33 ± 0.74%. Volume and part geometry also played an essential role in sintering outcome - while the big and upward standing slip cast cup in Fig. 5 showed severe bloating, slip cast samples sintered with the same schedule (but lying flat on the sinterplate) showed no bloating.

Water absorption differed significantly for the same samples using different absorption procedures. The short 10 min immersion is deemed fast and reliable for judging sintering density after each individual sintering run (directly after taken samples out of the oven and before setting the next sintering schedule). Two further procedures (24h immersion/procedure B and boiling in water/procedure C) were used to calculate a pore interconnectivity factor (A_x) introduced by Cultrone *et al.* [55]. For this, the free water absorption (A_l) with forced water absorption (A_f) was correlated using the following equation:

$$A_x = \frac{A_f - A_l}{A_f} \times 100\,\% \quad (1)$$

While samples with high interconnectivity (where A_f and A_l are similar) show low A_x values, samples with pores that are difficult to access (as these are only filled by forced water absorption) have high A_x values. Here, the free water absorption was obtained by 24h immersion and for forced water absorption immersion in boiling water after ISO 10545-3:1995 [37] was used. This is slightly different from Cultrone *et al.* [55], who used a vacuum procedure for A_f, which is deemed to have resulted in slightly higher water absorption values [56] (which would have resulted in higher A_x values here). A_x values were very high in the range from 42.30 to 73.50% which is indicative of low pore interconnectivity compared with A_x values found in literature of bricks made from clay with differing amounts of carbonates and sintered between 700 and 1100 °C which showed a very high to medium pore interconnectivity with A_x values from 2.06 to 21.26% (highest A_x values were found in samples fired at the highest temperatures) [55]. Only bricks made of 70% ball clay and 30% quartz sand and sintered at 900 °C that had been threaded with Silo 111 - an oligomeric organosiloxane water repellant (CTS Srl, Italy) - had similar values with A_x = 45.22% [57]. Here, the lowest pore interconnectivity was found for additively manufactured parts sintered in oxidizing atmosphere with robocasting at A_x = 73.50% and LSD 71.27% followed by slip casting with 65.42%.

Table 2
Linear sintering shrinkage of LSD-fabricated samples (see 3.1.2/3 for sintering conditions) chosen for mechanical tests in X/Y/Z directions. Data obtained from three samples in each direction.

Sample	Shrinkage in X (%)	Shrinkage in Y (%)	Shrinkage in Z (%)
LSD O_2	9.21 ± 0.42	10.08 ± 0.58	13.36 ± 0.82
LSD Mars	7.53 ± 0.02	8.89 ± 0.07	11.34 ± 0.01

In the general classification of ceramics MGS-1C/8 bodies in Table 1 fall into the category of crude stoneware with a water absorption between 4% and 8% (while fine stoneware has water absorption lower than 2% and fine pottery from 9% to 22%) [38]. ISO 13006 [58] classifies extruded and dry pressed tiles in three water absorption (ISO 10545-3) categories: Tiles with $A_f \leq 3\%$ fall in the category of low water absorption, tiles in between $3\% < A_f \leq 10\%$ in medium water absorption and $A_f > 10\%$ in high water absorption. Therefore, of the samples in Table 1, only robocast samples fall in the low water absorption category with A_f = 2.83 ± 0.03%, while all others have medium water absorption. This is significant, as ceramics with low water absorption ($A_f \leq 3\%$) are often cited as being frost-resistant [16]. However, some ceramics with higher absorption might withstand a sufficient number of freeze-thaw cycles depending on the application. Even though definitive results on frost behavior can only be obtained using special procedures such as normative ISO10545-12 [59], the authors hypothesize that MGS-1C/8 ceramics in Table 1 might have frost-resistance because of their low pore interconnectivity. This is significant, as on Mars (which has typical temperature swings of ~100 K), freeze-thaw resistance of building materials can be of great importance, which is illustrated by recent research indicating that freeze-thaw cycling on Mars acts as a chemical weathering agent [60].

3.1.5. Shrinkage and porosity of LSD samples

For the two sintering schedules selected for the mechanical tests, detailed sintering shrinkage analysis in X/Y/Z directions was conducted (Table 2), revealing anisotropic shrinkage typical for green bodies produced in powder bed processes.

Calculating a simple ratio by dividing Z values by X values, reveals a similar maximum shrinkage deviation ratio of Z/X = 1.451 for oxidizing atmosphere and Z/X = 1.506 in simulated Mars atmosphere. The authors assume that the larger standard deviation values for samples sintered in oxidizing atmosphere indicate a higher pyroplastic deformation, i.e., very mature bodies. As described in 2.3.3, such reproducible anisotropic shrinkage has been previously reported for porcelain and Al_2O_3 LSD samples, both with slightly higher shrinkage in Z-direction [3,5]. While

Table 3
Density and porosity determined by Archimedes' method and helium pycnometry of LSD-printed samples chosen for mechanical tests.

Sinter condition	Archimedes' bulk density ρ_{bulk} (g/cm^3)[a]	Whole disc pycn. density $\rho_{pycnometric}$ (g/cm^3)[b]	Ground powder pycn. density $\rho_{porefree}$ (g/cm^3)[b]	Total porosity volume V_{total} (%)	Open porosity volume V_{open} (%)	Closed porosity volume V_{closed} (%)
LSD O_2	2.54 ± 0.05	3.07 ± 0.03	3.09 ± 0.02	16.65 ± 0.2	15.98 ± 0.2	0.67 ± 0.002
LSD Mars	2.49 ± 0.02	3.00 ± 0.04	3.02 ± 0.01	17.59 ± 0.63	16.89 ± 0.64	0.70 ± 0.005

[a] Data obtained from three samples.
[b] Data obtained from five samples.

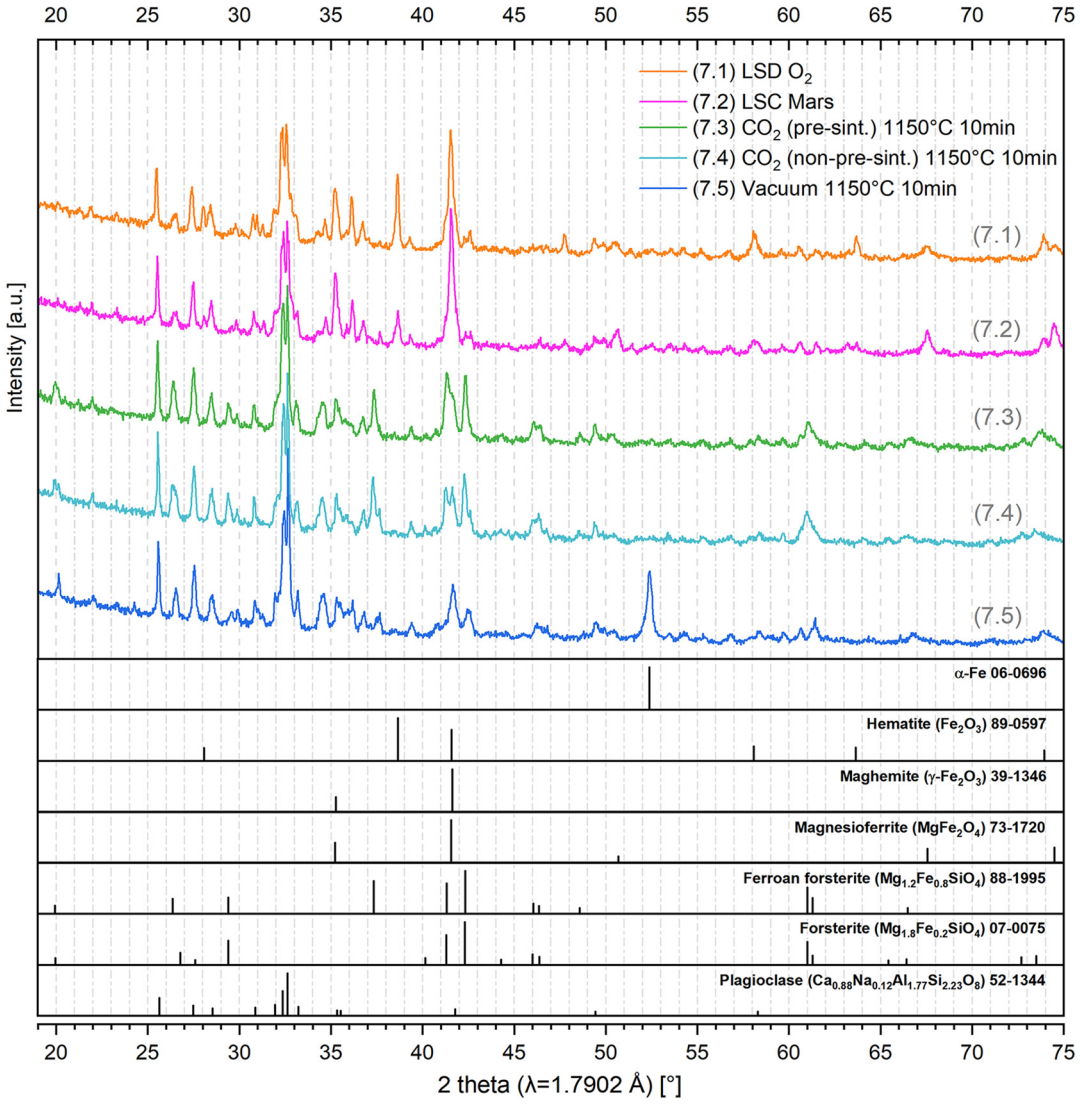

Fig. 6. In situ synchrotron XRD (λ = 0.49594 Å) patterns for LSD printed MGS-1C/8 heated from room temperature to 1200 °C at 10 K/min followed by cooling in two atmospheres: (a) in oxidizing atmosphere and (b) in simulated Mars atmosphere with 610 Pa partial pressure of CO_2.

alumina sintered at 1600 °C showed the lowest ratio between X and Z shrinkage with Z/X = 1.289 [17], compared to MGS-1C/8 porcelain showed an even higher ratio with Z/X = 1.698 [19]. The anisotropic shrinkage of LSD samples is likely related to the preferential orientation of the particles along the XY plane resulting from the layer deposition, as discussed, for example in Ref. [20]. This hypothesis is in agreement with the observation that the ratio Z/X is higher for porcelain, which typically contains a higher fraction of anisotropic (elongated or platelet-like) particles compared to alumina. In general, shrinkage for MGS-1C/8 samples sintered in ambient air was similar to LSD porcelain samples (with deviations in Z-direction) [19]. Issues relating to anisotropic shrinkage in the LSD process can easily be overcome, as shrinkage is reproducible (for bodies with low pyroplastic deformation) and 3D geometries can easily be adjusted during the design and preparation process.

Even though MGS-1C/8 shrinkage was generally on a par with LSD porcelain, total porosity was slightly higher, with 16.65 ± 0.2% in oxidizing and 17.59 ± 0.63% in simulated Mars atmosphere (Table 3), compared to a total porosity of 8.79 ± 0.2% for porcelain [19].

However, open and closed porosity were inverted as MGS-1C/8

Fig. 7. Ex situ XRD patterns of LSD disc samples sintered under different temperatures and atmospheric conditions, including samples 7.1 (LSD O_2) and 7.2 (LSD Mars) used for the characterization of mechanical properties.

samples showed almost exclusively open porosity, while closed porosity was prevalent for porcelain LSD samples [19]. There were slight differences for true powder density for oxidizing and Mars atmosphere, which could be related to a mass gain from oxidation. Furthermore, the presence of iron with high atomic weight in MGS-1C/8 is likely responsible for significantly higher true density (3.02–3.09 g/cm^3) compared to porcelain feedstock (that typically has below 1 wt% iron) with 2.59 g/cm^3.

3.2. Phase composition, microstructure and mechanical properties of sintered LSD samples

3.2.1. Phase evolution from in situ heating XRD studies

As already indicated by differing sintering behavior and color change, marked differences in the phase evolution (for the original composition of MGS-1 see 2.1) during sintering of MGS-1C/8 for oxidizing and simulated Mars atmosphere was observed (Fig. 6).

For both panels in Fig. 6, reflections shift to lower angles upon heating due to thermal expansion of the crystals lattice. A subsequent lattice contraction upon cooling leads to a shift back to the original position of the reflections at higher 2 theta values. The MGS-1C/8 silicate constituents were discussed in detail in our previous study [5], here we focus on phase evolution during sintering in both atmospheres. First, the drying of the clay component is observed through the reduction of sodium montmorillonite d_{001} spacing towards smaller distances. The basal spacing associated with 12 water molecules per exchangeable cation for montmorillonite is ~16 Å at room temperature [5], which is also what is observed here (d_{001} = 16.15 Å). As the amount of interlayer water is reduced in oxidizing atmosphere, a jump first to 12.76 Å around 420 °C with a second shift back to 13.94 Å at 660 °C is observed, which is associated with a lower hydration state with 6 water molecules per cation. In simulated Martian conditions, no second shift was observed, with the switch to the lower hydration state around 420 °C to 13.34 Å and the complete disappearance of the corresponding reflection at 2.13 2theta starting around 900 °C, the latter can be associated with the melting of the clay component.

For both atmospheres, the most apparent phase changes are related to different iron-containing compounds. XRF analysis of MGS-1C/8 by the authors revealed that the starting simulant contained 11.25 wt% FeO_T in sum [5]. This, in turn, is comprised of various iron-containing compounds in the MGS-1 powders, i.e., 1.9 wt% magnetite (Fe_3O_4), 1.1 wt% hematite (Fe_2O_3), 1.7 wt% ferrihydrite ($Fe^{3+}{}_{10}O_{14}(OH)_2$) and 1.4 wt% Fe-carbonate/crystalline siderite ($FeCO_3$) [29], as well as silicate minerals. Looking at the phase evolution during sintering in oxidizing atmosphere (Fig. 6a), the most prominent phase change is the formation of hematite. During heating starting from 800 °C, a significant intensification of hematite reflections can be observed, ending with very strong hematite reflections after cooling. Furthermore, during holding at 1200 °C, a strong appearance of cristobalite (SiO_2) reflections can be observed, which also prevails until after cooling. As no cristobalite was observed in ex situ experiments (see 3.2.2), this cristobalite formation most probably stems from the quartz capillary used as sample holder undergoing a phase transformation, something observed here for this setup. Cristobalite formation is typical for non-vitreous stoneware bodies with high iron content. During sintering, cristobalite formation can be an important consideration, especially when envisioning applications, as the cristobalite inversion is in a low-temperature region (100–270 °C). This inversion coincides with a marked volume change, which is different from the alpha-beta inversion of quartz found in porcelains that do not form cristobalite.

The 5 wt% clay content in MGS-1 did have a small effect on MGS-1C/8 sintering behavior in oxidizing atmosphere (see Supplementary Fig. 1), as unprocessed MGS-1 without clay had almost identical phase

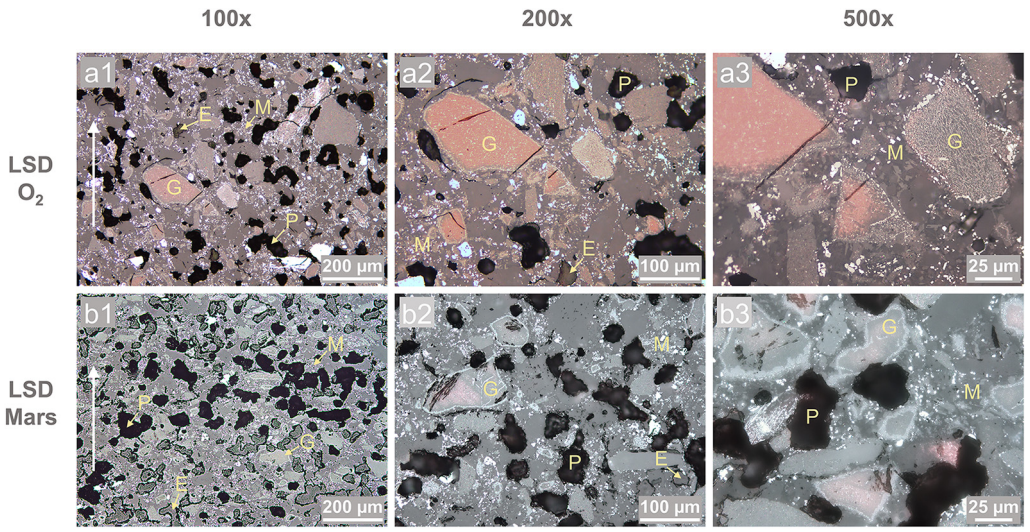

Fig. 8. Optical micrographs of polished crosssections of LSD O2 and LSD Mars samples. The white arrow on the left indicates LSD Z-direction. G represents the mineral grains, M represents the matrix from liquid phase sintering, E represents epoxy-filled pores and P represents pores not infiltrated by the mounting epoxy.

composition only with hematite reflections slightly smaller while cristobalite reflections were stronger compared with MGS-1C/8.

In situ sintering in simulated Mars atmosphere (here, at 610 Pa CO_2 partial pressure with N_2 as filler) produced markedly different phases, with the most intense reflections from the formation of metallic iron phases and carbon raised from the decomposition of the binder. It appears that the heating in the in situ XRD sample environment leads to the reduction of the iron-containing constituents. This effect was not observed in the ex situ studies (see 3.2.2). Hematite reflections with low intensity present at room temperature begin to disappear around 500 °C and are gone at 820 °C, where the formation of γ-iron (austenite) starts, which prevails during the 1200 °C dwell time until when the intensity of the γ-iron reflections begin to decrease during cooling with the emergence of the reflections assigned to α-iron (ferrite) starting around 900 °C. Finally, at room temperature, no γ-iron and strong α-iron reflections are observed.

3.2.2. *Phase composition of sintered LSD samples*

Compared to in situ XRD results, LSD samples (for original MGS-1 phase composition see 2.1) sintered in a furnace with open heating elements in ambient air (7.1) and a tube furnace under different atmospheric conditions (7.2–7.5) produced slightly different results (Fig. 7).

On the one hand, this could stem from slow heating and cooling (1.7 K/min) with long holding times, as well as from the divergence of how Mars atmosphere was simulated, as the tube furnace could be sealed and run below 1 bar, which was not possible for the in situ XRD setup, for which a gas stream of N_2 with CO_2 simulating Martian CO_2 partial pressure was used. Another factor that could have influenced phase composition is sintering geometry - while in situ experiments were conducted with samples in powder form (with gas streaming through the powder), ex situ measurements were performed using green body discs (with possibly less gas/solid interaction). In sum, this led to markedly different phases, as none of the parts sintered in CO_2 atmospheres in the sealed tube furnace (7.2–7.4) produced metallic iron, indicating that the gas flow had higher reduction potential compared to standing CO_2 atmosphere. However, continually applying vacuum during sintering seemed to have similar reduction potential, as the XRD patterns of LSD samples sintered under such conditions (7.5) display intensive α-iron reflections (comparable in the intensity to those in the in situ XRD pattern results under N_2/CO_2 gas stream) with forsterite ($Mg_{1.2}Fe_{0.8}SiO_4$) and plagioclase reflections that are shared by all samples (7.2–7.5). The phase composition of the pre-sintered and non-pre-sintered sample (7.4) and (7.3) was mostly similar, with iron mainly in ferroan forsterite ($Mg_{1.2}Fe_{0.8}SiO_4$) in the 2+ oxidation state, as well as in maghemite/magnetite. Magnetite and maghemite cannot be distinguished, as their XRD patterns are identical [61]. However, as samples were stored in air, maghemite is assumed. Holding at high temperature in the same atmosphere (7.2) produced samples with no detectable forsterite, resulting in the formation of a magnesioferrite phase (previously discussed in 3.1.3) belonging to the spinel group, a maghemite phase and some hematite. The same phases were detected for samples sintered in oxidizing atmosphere (7.1) except for more intense hematite reflections. Comparing with ISRU sintering studies in simulated atmospheres of a variety of different lunar simulants mentioned in the introduction, it is interesting to note that for sintering in vacuum, no metallic iron phase was reported [21,22]. On the other hand, a hydrogen atmosphere has been reported to reduce ilmenite ($FeTiO_3$) to metallic iron during sintering [23] and oxygen deprivation from argon was the proposed reason why sintering of lunar simulants resulted in a metallic iron phase [24].

3.2.3. *Microstructure of sintered LSD parts*

LSD parts sintered in oxidizing and simulated Mars atmosphere showed a heterogeneous microstructure typical for clay-based ceramics (Fig. 8).

As shown in the previous sections by discussing water absorption, density and porosity measurements, LSD samples sintered under simulated Mars atmosphere showed a slightly higher number of pores that also tended to be interconnected, which corresponds to the pore interconnectivity values obtained (Table 1). Higher pore interconnectivity is also apparent from the vacuum epoxy infiltration, as almost all pores at the edges of the disc were filled (only the center of the disc showed non-filled pores) for simulated Mars atmosphere samples (b1), which was not the case for LSC O_2 sample sintered in oxidizing atmosphere (a1), where few pores were filled. For both samples (a2, b2) this matrix is comprised of a melt phase from liquid phase sintering, probably containing the montmorillonite particles which form a liquid phase between 950 and 1050 °C [39]. This matrix is dotted with smaller whiteish particles which judging from EDX results of similar parts [21,23] are assumed to be the iron-containing phases. At higher magnifications (a3, b3), the matrix can be seen to have been devitrified as a crystal texture for both atmosphere becomes visible, which coincides with the phase analysis (Fig. 7), where no significant amorphous phase was found. With white arrows in (a1) and (a2) indicating Z-direction in the LSD prints, no interface between layers from the LSD process was visible after sintering neither for (a1) nor for (b1). This is in line with what has been reported before [17,19] and is an important advantage of the LSD process in general.

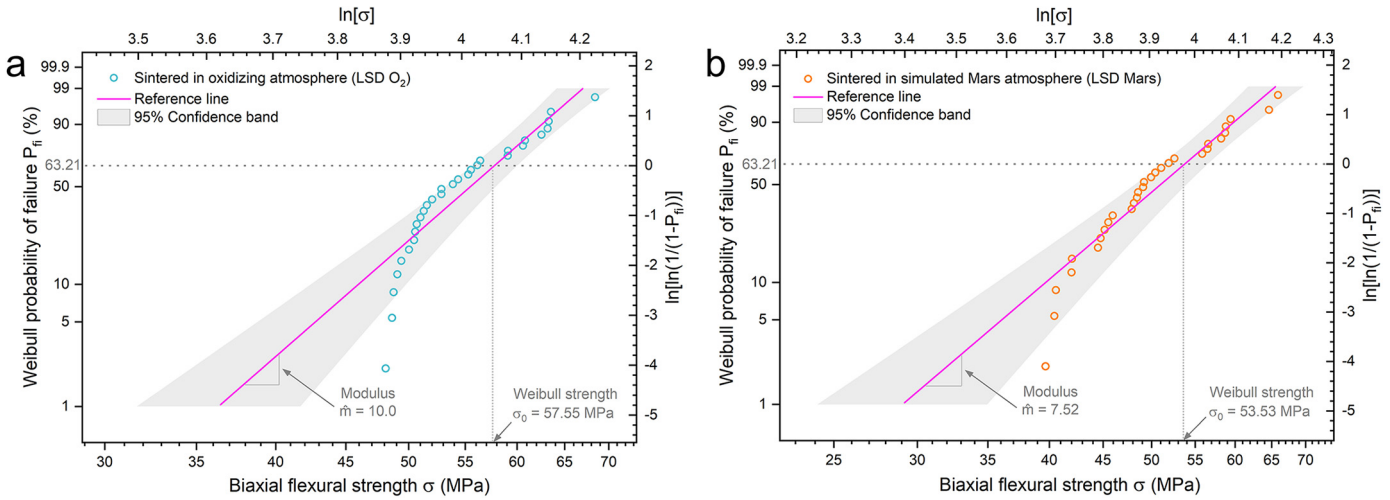

Fig. 9. Weibull fracture probability plots for the ball on three balls biaxial bending of samples printed in XY plane: (a) LSD O_2, (b) LSD Mars.

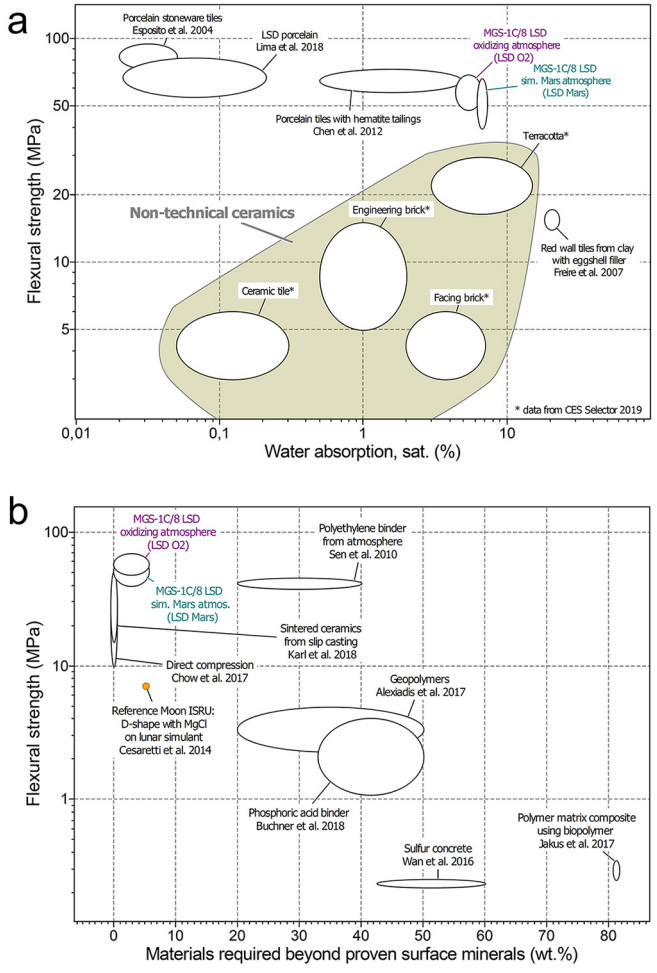

Fig. 10. (a) Flexural strength over water absorption for ceramic materials in common use on Earth and (b) flexural strength over additional materials required (aside from regolith and clay minerals) for Mars ISRU material systems and one reference study for Moon ISRU (all references mentioned in the text).

3.2.4. Mechanical properties

With phase composition and microstructure similar to vitreous clay ceramics (see Figs. 7 and 8), the flexural strength of MGS-1C/8 ceramics (measured using ball on three balls method) sintered both in oxidizing and simulated Mars atmosphere was in a comparable range to typical crude stoneware (Fig. 9).

For the 30 LSD O_2 samples with 15.98 ± 0.2% apparent porosity, the Weibull characteristic strength was $\sigma_0 = 57.55$ MPa and for 30 LSD Mars samples with 16.89 ± 0.64% apparent porosity (Table 3) it was 53.53 MPa. This is slightly lower than the 76.3 MPa reported by Lima *et al.* for XY plane LSD prints made of soft porcelain sintered higher at 1250 °C which can be explained by the unique properties of porcelain and by the lower amounts of pores (apparent porosity of 0.27 ± 0.22% and a closed porosity of 8.52 ± 1.22%) [19]. Both samples had decent Weibull modulus with $\hat{m} = 10.0$ for LSD O_2 and $\hat{m} = 7.52$ for LSD Mars samples, which is as well slightly lower compared with LSD prints in XY direction that had 14.4 [19].

3.2.5. Comparison with terrestrial ceramics and evaluation against various ISRU material concepts

Compared with ceramic materials in common use on Earth, sintered MGS-1C/8 LSD printed discs showed bending strength between terracotta and typical porcelains (Fig. 10a).

While typical non-technical ceramics such as terracotta, engineering brick, facing brick and ceramic tile had less than half the flexural strength, various porcelains, including red porcelain tiles with hematite tailings (instead of traditional fluxes) [62]. LSD porcelain [19] and porcelain stoneware tiles with nepheline-syenite as fluxing agent [63], had slightly higher flexural strength. In comparison, water absorption for MGS-1C/8 discs was only surpassed by a study for red wall tiles filled with eggshell waste [64], while on par with average water absorption for earthenware, such as terracotta and slightly higher than facing brick, a common building material. All other ceramics had lower water absorption making them either waterproof/not to leak liquids or deteriorate in freeze/thaw conditions. The authors propose two possible routes to watertight ISRU ceramics: On the one hand, the feedstock composition could be adjusted and components, that bloat could be reduced, which would enable dense sintered ISRU stoneware. On the other hand, the ceramics presented here could be glazed by developing an ISRU glaze employing minerals commonly found on Mars as fluxes.

Comparing with other studies on ISRU material system for Mars the authors are aware of (see Fig. 10b), all other materials and processing approaches reported lower flexural strength with higher weight fraction of non-ISRU materials needed, which would have to be shipped, synthesized or extracted (except for a study on direct compression, which exclusively used regolith [65]). Of the three other additive manufacturing studies in Fig. 10b the reference Moon ISRU on binder jetting of lunar regolith using the D-shape technology had the highest flexural strength while only

requiring a low amount of magnesium salt binder to be shipped [66]. This was followed by material extrusion using a phosphoric acid of which 33% would have to be shipped [15] and a study using mainly biopolymers and organic solvents to produce polymer regolith composites for which over 80 wt% of complex organic materials would have to be shipped [14]. For ISRU material concepts in general, the study on direct compression (which exclusively used regolith), produced high flexural strength [65], very similar for a study from the authors that used slip casting and sintering (that also only required regolith) [36]. The polymer composites via the ISRU production of polyethylene binder (20–40 wt%) similarly produced high flex strength [67], while concepts for geopolymers [68] and sulfur concrete [69] are deemed more suited for structures utilized in compression.

Contrary to this, no shipping or synthesis of material would be required to produce sintered ceramics from clay green bodies. What is more, wet processing of ceramics can be done without the 0.5 wt% dispersant, currently added [5] and if techniques other than LSD are used, no binder would be required. To assess the usefulness of different ISRU material systems on Mars, it is proposed that the use on Earth is an important indicator, assuming material systems with good material availability, easy processing and favorable properties prevailed on Earth over others. Except for geopolymers and sulfur concrete, most of the material and processing proposals in Fig. 10b are not used on a bigger scale on Earth. Contrary to this, sintered ceramics - one of the earliest human inventions (originating before the Neolithic period) - has been and still is a universal tool employed all over the world on a large industrial scale. Similar to traditional basic processing for clay-based materials on Earth, realistic early clay ISRU for sintered ceramics could employ deformation of clay bodies for press molding of mud bricks/adobe bricks or material extrusion which is widely used on Earth for bricks and tiles. Furthermore, the additive manufacturing version of material extrusion, robocasting/direct ink writing, could be used to produce more complex geometries making clay ISRU for sintered ceramics an eminently favorable construction technology for soft and hard ISRU on Mars.

3.2.6. *Suggestions for future Martian ceramics*

While smectite minerals are favorable for high green body strength and suitable slurry viscosity at low smectite percentages, high strength and dense-fired ceramics such as porcelain typically make use of kaolinite clays, that are also present on Mars [3]. Subsequent ISRU scenarios could aim to manufacture such more advanced ceramics. The authors propose purification and enrichment of raw kaolinite in two steps, similar to what is done for kaolin on Earth: First, removal of unwanted materials (such as carbonates and iron oxides) by physical or chemical means and second fractionation by sedimentation to facilitate the removal of remaining impurities (such as quartz). For the production of a Martian hard-paste porcelain, such kaolin would be mixed with feldspar and quartz resources found on Mars [70], wet-milled, shaped, dried and fired at temperatures around 1400 °C. In the absence of organic material resources and the complexity of producing metals, such gas-tight fired porcelain could be a viable material system for the manufacture of a great variety of parts needed for the exploration and colonization of Mars.

4. Conclusions

In this work, the feasibility of sintering Mars global simulant for clay ISRU green bodies shaped using four different wet processing approaches and a dry-pressed reference was demonstrated. The thermal behavior and properties of green bodies during and after sintering was extensively characterized and two sintering schedules aiming for dense parts without excess pyroplastic deformation in two different atmospheric conditions (one in ambient Earth atmosphere and one in simulated Martian atmosphere) were developed. Sintered ceramics showed low water absorption and excellent mechanical properties with bending strength between terracotta and porcelain. However, the sintering experiments for discs were undertaken with oven locations carefully mapped and calibrated because of the small sintering interval. For large scale production, clay bodies are often purposely sintered at temperatures less than mature to get more stability in the kiln and sufficient firing margin for incorrect firing, which is what the authors propose for the sintering of larger parts. If dense parts are required, adjustments to raw material chemistry are proposed, for example, by adding minerals that act as fluxes, which would allow dense sintering at temperature before the onset of bloating. Here, the versatile robocasting additive manufacturing technology produced parts with the lowest water absorption and the authors foresee a multitude of applications for clay products such as Martian pottery/sintered ceramics in hard and soft ISRU on Mars.

Declaration of competing interests

The authors declare that they have no known competing financial interests or personal relationships that could have appeared to influence the work reported in this paper.

Acknowledgment

David Karl would like to thank the Evonik Stiftung for their financial support. We thank Mathias Czasny TU Berlin for retrofitting an Ultimaker printer with the robocasting setup. We thank Dagmar Nicolaides for HSM, Heidi Marx for polishing samples (both BAM) and Heinz Sap TU Berlin for TG. Furthermore, we are grateful to Exolith lab for supplying simulants and their service to the ISRU community in general. This research used resources of the Advanced Light Source, which is a DOE Office of Science User Facility under contract no. DE-AC02-05CH11231. Furthermore, we acknowledge support by the German Research Foundation and the Open Access Publication Funds of TU Berlin.

Appendix A. Supplementary data

Supplementary data to this article can be found online at https://doi.org/10.1016/j.oceram.2020.100008.

References

[1] K.M. Cannon, D.T. Britt, Feeding one million people on Mars, New Space 7 (2019) 245–254, https://doi.org/10.1089/space.2019.0018.
[2] J.J. Wray, S.T. Hansen, J. Dufek, G.A. Swayze, S.L. Murchie, F.P. Seelos, J.R. Skok, R.P. Irwin, M.S. Ghiorso, Prolonged magmatic activity on Mars inferred from the detection of felsic rocks, Nat. Geosci. 6 (2013) 1013–1017, https://doi.org/10.1038/NGEO1994.
[3] B.L. Ehlmann, C.S. Edwards, Mineralogy of the martian surface, Annu. Rev. Earth Planet Sci. 42 (2014) 291–315, https://doi.org/10.1146/annurev-earth-060313-055024.
[4] N.K. Ramkissoon, V.K. Pearson, S.P. Schwenzer, C. Schröder, T. Kirnbauer, D. Wood, R.G.W. Seidel, M.A. Miller, K. Olsson-Francis, New simulants for martian regolith: controlling iron variability, Planet. Space Sci. (2019) 104722, https://doi.org/10.1016/j.pss.2019.104722.
[5] D. Karl, T. Duminy, P. Lima, F. Kamutzki, A. Gili, A. Zocca, J. Günster, A. Gurlo, Clay in situ resource utilization with Mars global simulant slurries for additive manufacturing and traditional shaping of unfired green bodies, Acta Astronaut. 174 (2020) 241–253, https://doi.org/10.1016/j.actaastro.2020.04.064.
[6] K.M. Cannon, D.T. Britt, T.M. Smith, R.F. Fritsche, D. Batcheldor, Mars global simulant MGS-1: a Rocknest-based open standard for basaltic martian regolith simulants, Icarus 317 (2019) 470–478, https://doi.org/10.1016/j.icarus.2018.08.019.
[7] A. Heath, D. Maskell, P. Walker, M. Lawrence, C. Fourie, Modern earth masonry: structural properties and structural design, Struct. Eng. 90 (2012) 38–44. http://www.istructe.org/webtest/files/60/6093d338-aa24-4ff8-8de5-99bc757940f8.pdf. (Accessed 20 December 2019).
[8] B. Khoshnevis, Automated construction by contour crafting—related robotics and information technologies, Autom. ConStruct. 13 (2004) 5–19, https://doi.org/10.1016/j.autcon.2003.08.012.
[9] B. Kading, J. Straub, Utilizing in-situ resources and 3D printing structures for a manned Mars mission, Acta Astronaut. 107 (2015) 317–326, https://doi.org/10.1016/j.actaastro.2014.11.036.
[10] M. Morris, C. Ciardullo, K. Lents, J. Montes, O. Rudakevych, M. Sono, Y. Sono, M. Yashar, Mars ice house: using the physics of phase change in 3D printing a habitat with H2O, in: AIAA Space, American Institute of Aeronautics and

Astronautics, Long Beach, California, 2016, p. 211, https://doi.org/10.2514/6.2016-5528.
[11] K.D. Grossman, T.S. Sakthivel, L. Sibille, J.G. Mantovani, S. Seal, Regolith-derived ferrosilicon as a potential feedstock material for wire-based additive manufacturing, Adv. Space Res. 63 (2019) 2212–2219, https://doi.org/10.1016/j.asr.2018.12.002.
[12] R.P. Mueller, S. Howe, D. Kochmann, H. Ali, C. Andersen, H. Burgoyne, W. Chambers, R. Clinton, X. de Kestellier, et al., Automated additive construction (AAC) for earth and space using in situ resources, in: R.B. Malla, J.H. Agui, P. van J. Susante (Eds.), Earth and Space 2016: Engineering for Extreme Environments, American Society of Civil Engineers, Reston, 2017, pp. 354–377, https://doi.org/10.1061/9780784479971.036.
[13] A. Goulas, R.A. Harris, R.J. Friel, Additive manufacturing of physical assets by using ceramic multicomponent extra-terrestrial materials, Addit. Manuf. 10 (2016) 36–42, https://doi.org/10.1016/j.addma.2016.02.002.
[14] A.E. Jakus, K.D. Koube, N.R. Geisendorfer, R.N. Shah, Robust and elastic lunar and martian structures from 3D-printed regolith inks, Sci. Rep. 7 (2017) 44931, https://doi.org/10.1038/srep44931.
[15] C. Buchner, R.H. Pawelke, T. Schlauf, A. Reissner, A. Makaya, A new planetary structure fabrication process using phosphoric acid, Acta Astronaut. 143 (2018) 272–284, https://doi.org/10.1016/j.actaastro.2017.11.045.
[16] C. Binggeli, Materials for Interior Environments, John Wiley & Sons, Hoboken, N.J., 2008.
[17] A. Zocca, P. Lima, J. Günster, LSD-based 3D printing of alumina ceramics, J. Ceram. Sci. Technol. 8 (2017) 141–147, https://doi.org/10.4416/JCST2016-00103.
[18] T. Muehler, C. Gomes, M.E. Ascheri, D. Nicolaides, J.G. Heinrich, J. Guenster, Slurry-based powder beds for the selective laser sintering of silicate ceramics: journal of ceramics science and technology, J. Ceram. Sci. Technol. 6 (2015) 113–117, https://doi.org/10.4416/JCST2015-0007.
[19] P. Lima, A. Zocca, W. Acchar, J. Günster, 3D printing of porcelain by layerwise slurry deposition, J. Eur. Ceram. Soc. 38 (2018) 3395–3400, https://doi.org/10.1016/j.jeurceramsoc.2018.03.014.
[20] A. Zocca, P. Lima, S. Diener, N. Katsikis, J. Günster, Additive manufacturing of SiSiC by layerwise slurry deposition and binder jetting (LSD-print), J. Eur. Ceram. Soc. 39 (2019) 3527–3533, https://doi.org/10.1016/j.jeurceramsoc.2019.05.009.
[21] A. Meurisse, J.C. Beltzung, M. Kolbe, A. Cowley, M. Sperl, Influence of mineral composition on sintering lunar regolith, J. Aero. Eng. 30 (2017) 4017014, https://doi.org/10.1061/(ASCE)AS.1943-5525.0000721.
[22] M. Fateri, A. Meurisse, M. Sperl, D. Urbina, H.K. Madakashira, S. Govindaraj, J. Gancet, B. Imhof, W. Hoheneder, et al., Solar sintering for lunar additive manufacturing, J. Aero. Eng. 32 (2019) 4019101, https://doi.org/10.1061/(ASCE)AS.1943-5525.0001093.
[23] S.L. Taylor, A.E. Jakus, K.D. Koube, A.J. Ibeh, N.R. Geisendorfer, R.N. Shah, D.C. Dunand, Sintering of micro-trusses created by extrusion-3D-printing of lunar regolith inks, Acta Astronaut. 143 (2018) 1–8, https://doi.org/10.1016/j.actaastro.2017.11.005.
[24] R. Dou, W.Z. Tang, L. Wang, S. Li, W.Y. Duan, M. Liu, Y.B. Zhang, G. Wang, Sintering of lunar regolith structures fabricated via digital light processing, Ceram. Int. 45 (2019) 17210–17215, https://doi.org/10.1016/j.ceramint.2019.05.276.
[25] H.B. Franz, M.G. Trainer, C.A. Malespin, P.R. Mahaffy, S.K. Atreya, R.H. Becker, M. Benna, P.G. Conrad, J.L. Eigenbrode, et al., Initial SAM calibration gas experiments on Mars: quadrupole mass spectrometer results and implications, Planet. Space Sci. 138 (2017) 44–54, https://doi.org/10.1016/j.pss.2017.01.014.
[26] R.E. Arvidson, P. Bellutta, F. Calef, A.A. Fraeman, J.B. Garvin, O. Gasnault, J.A. Grant, J.P. Grotzinger, V.E. Hamilton, et al., Terrain physical properties derived from orbital data and the first 360 sols of Mars Science Laboratory Curiosity rover observations in Gale Crater, J. Geophys. Res. Planets 119 (2014) 1322–1344, https://doi.org/10.1002/2013JE004605.
[27] Centro de Astrobiología (CSIC-INTA), REMS team, Rover environmental Monitoring station, pressure measurements: Mars science laboratory (NASA). http://cab.inta-csic.es/rems/marsweather.html. (Accessed 16 April 2020).
[28] R.M. Haberle, Solar systems/sun, atmospheres, evolution of atmospheres | Planetary atmospheres, in: Encyclopedia of Atmospheric Sciences, Elsevier, 2015, pp. 168–177, https://doi.org/10.1016/B978-0-12-382225-3.00312-1.
[29] CLASS Exolith Lab, in: Kevin M. Cannon, Mike Conroy, Daniel T. Britt (Eds.), Datasheet for MGS-1 Mars Global Simulant, University of Central Florida, USA, March 2019. https://sciences.ucf.edu/class/simulant_marsglobal. (Accessed 20 April 2020).
[30] CLASS Exolith Lab, in: Kevin M. Cannon, Mike Conroy, Daniel T. Britt (Eds.), Datsheet for MGS-1C Clay ISRU, University of Central Florida, USA, November 2018. https://sciences.ucf.edu/class/simulant_mgs1c. (Accessed 18 April 2020).
[31] D.L. Bish, D.F. Blake, D.T. Vaniman, S.J. Chipera, R.V. Morris, D.W. Ming, A.H. Treiman, P. Sarrazin, S.M. Morrison, et al., X-ray diffraction results from Mars science laboratory: mineralogy of rocknest at Gale Crater, Science (New York, N.Y.) 341 (2013) 1238932, https://doi.org/10.1126/science.1238932.
[32] A. Abbud-Madrid, D. Beaty, D. Boucher, B. Bussey, R. Davis, L. Gertsch, et al., Mars Water In-Situ Resource Utilization (ISRU) Planning (M-WIP) Study: 90 P, California Insitute of Technology, April 2016. Posted, https://mepag.jpl.nasa.gov/reports/Mars_Water_ISRU_Study.pdf. (Accessed 20 April 2020).
[33] T.F. Bristow, E.B. Rampe, C.N. Achilles, D.F. Blake, S.J. Chipera, P. Craig, J.A. Crisp, D.J. Des Marais, R.T. Downs, et al., Clay mineral diversity and abundance in sedimentary rocks of Gale crater, Mars, Sci. Adv. 4 (2018), https://doi.org/10.1126/sciadv.aar3330 eaar3330.
[34] S. Rasche, S. Strobl, M. Kuna, R. Bermejo, T. Lube, Determination of strength and fracture toughness of small ceramic discs using the small punch test and the ball-on-three-balls test, Procedia Mater. Sci. 3 (2014) 961–966, https://doi.org/10.1016/j.mspro.2014.06.156.
[35] D.C. Snell, C.H. Lager, Economic Texts from Sumer, Yale University Press, 1992, https://doi.org/10.2307/j.ctt2250x31.
[36] D. Karl, F. Kamutzki, A. Zocca, O. Goerke, J. Guenster, A. Gurlo, Towards the colonization of Mars by in-situ resource utilization: slip cast ceramics from Martian soil simulant, PloS One 13 (2018), e0204025, https://doi.org/10.1371/journal.pone.0204025.
[37] ISO, Ceramic Tiles - Part 3: Determination of Water Absorption, Apparent Porosity, Apparent Relative Density and Bulk Density; (Reference Number: ISO 10545-3: 1995(E)), 1995.
[38] ISO, Fine Ceramics (Advanced Ceramics, Advanced Technical Ceramics) - Determination of Density and Apparent Porosity; (Reference Number: ISO 18754: 2013(E)), 2013.
[39] F.J. Semel, D.A. Lados, Porosity analysis of PM materials by helium pycnometry, Powder Metall. 49 (2006) 173–182, https://doi.org/10.1179/174329006X95347.
[40] A. Doran, L. Schlicker, C.M. Beavers, S. Bhat, M.F. Bekheet, A. Gurlo, Compact low power infrared tube furnace for in situ X-ray powder diffraction, Rev. Sci. Instrum. 88 (2017) 13903, https://doi.org/10.1063/1.4973561.
[41] L. Schlicker, A. Doran, P. Schneppmüller, A. Gili, M. Czasny, S. Penner, A. Gurlo, Transmission in situ and operando high temperature X-ray powder diffraction in variable gaseous environments, Rev. Sci. Instrum. 89 (2018) 33904, https://doi.org/10.1063/1.5001695.
[42] A.P. Dhupe, A.N. Gokarn, Studies in the thermal decomposition of natural siderites in the presence of air, Int. J. Miner. Process. 28 (1990) 209–220, https://doi.org/10.1016/0301-7516(90)90043-X.
[43] C.M. Riley, Relation of chemical properties to the bloating of clays, J. Am. Ceram. Soc. 34 (1951) 121–128, https://doi.org/10.1111/j.1151-2916.1951.tb11619.x.
[44] H.S. Wilson, Lightweight Aggregates: Properties, Applications and Outlook, 79–33, Canada Centre for Mineral and Energy Technology, 1979, pp. 1–23, https://doi.org/10.4095/307188. Minerals, CANMET Report.
[45] B.L. Sherriff, C. McCammon, L. Stirling, A Mössbauer study of the color of Roman pottery from the Leptiminus archaeological site, Tunisia, Geoarchaeology 17 (2002) 863–874, https://doi.org/10.1002/gea.10044.
[46] O. Opuchovic, A. Kareiva, Historical hematite pigment: synthesis by an aqueous sol–gel method, characterization and application for the colouration of ceramic glazes, Ceram. Int. 41 (2015) 4504–4513, https://doi.org/10.1016/j.ceramint.2014.11.145.
[47] A. de Bonis, G. Cultrone, C. Grifa, A. Langella, A.P. Leone, M. Mercurio, V. Morra, Different shades of red: the complexity of mineralogical and physico-chemical factors influencing the colour of ceramics, Ceram. Int. 43 (2017) 8065–8074, https://doi.org/10.1016/j.ceramint.2017.03.127.
[48] U. Schwertmann, R.M. Cornell, Iron Oxides in the Laboratory: Preparation and Characterization, 2., Completely Rev. And Extended, e, Wiley-VCH, Weinheim, 2008 d., 2. reprint.
[49] W.R. Morgan, Oxidation and Loss of Weight of Clay Bodies during Firing; a Report of an Investigation Conducted by the Engineering Experiment Station, University of Illinois in cooperation with the Clay Products Association, 1936. http://hdl.handle.net/2142/4389. (Accessed 20 April 2020).
[50] W.E. Brownell, Black coring in structural clay products, J. Am. Ceram. Soc. 40 (1957) 179–187, https://doi.org/10.1111/j.1151-2916.1957.tb12600.x.
[51] W.E. Brownell, Structural Clay Products, Springer Vienna, Vienna, 1976.
[52] M. Maggetti, G. Galetti, H. Schwander, M. Picon, R. Wessicken, Campanian pottery; the nature of the black coating, Archaeometry 23 (1981) 199–207, https://doi.org/10.1111/j.1475-4754.1981.tb00306.x.
[53] C.T. Grimm, Durability of brick masonry: a review of the literature, in: J.C. Grogan, J.T. Conway (Eds.), Masonry: Research, Application, and Problems, ASTM International, 1985, https://doi.org/10.1520/STP34557S, 202-202-33.
[54] G. Marchal, Action of silica on barium and magnesium sulphates, in: R.O. Purdy, E.C. Sohoick (Eds.), Ceramic Abstracts Compiled by the Amercian Ceramic Society, 1926, https://doi.org/10.1111/j.1151-2916.1926.tb18320.x.
[55] G. Cultrone, E. Sebastián, K. Elert, M.J. de La Torre, O. Cazalla, C. Rodriguez–Navarro, Influence of mineralogy and firing temperature on the porosity of bricks, J. Eur. Ceram. Soc. 24 (2004) 547–564, https://doi.org/10.1016/S0955-2219(03)00249-8.
[56] A.W. Vieira, M.D.d.M. Innocentini, E. Mendes, T. Gomes, A. Demarch, O.R.K. Montedo, E. Angioletto, Comparison of methods for determining the water absorption of glazed porcelain stoneware ceramic tiles, Mat. Res. 20 (2017) 637–643, https://doi.org/10.1590/1980-5373-mr-2017-0089.
[57] G. Cultrone, F. Madkour, Evaluation of the effectiveness of treatment products in improving the quality of ceramics used in new and historical buildings, J. Cult. Herit. 14 (2013) 304–310, https://doi.org/10.1016/j.culher.2012.08.001.
[58] ISO, Ceramic Tiles - Definitions, Classification, Characteristics and Marking; (Reference Number: ISO 13006:2018(E)), 2018.
[59] DIN EN ISO, Ceramic Tiles Part 12: Determination of Frost Resistance; (Reference Number: EN ISO 10545-12:1997), 1997.
[60] N.A. Scudder, B. Horgan, R.J. Smith, A. Rutledge, E.B. Rampe, Freeze-Thaw Cycling as a Chemical Weathering Agent on a Cold and Icy Mars, 51st Lunar and Planetary Science Conference (LPSC), The Woodlands, TX; United States, 2020. March 16, 2020 - March 20, 2020, https://ntrs.nasa.gov/search.jsp?R=20200001879. (Accessed 5 May 2020).
[61] A. Kotoulas, C. Dendrinou-Samara, M. Angelakeris, O. Kalogirou, The effect of polyol composition on the structural and magnetic properties of magnetite nanoparticles for magnetic particle hyperthermia, Materials (Basel, Switzerland) 12 (2019), https://doi.org/10.3390/ma12172663.
[62] Y. Chen, Y. Zhang, T. Chen, T. Liu, J. Huang, Preparation and characterization of red porcelain tiles with hematite tailings, Construct. Build. Mater. 38 (2013) 1083–1088, https://doi.org/10.1016/j.conbuildmat.2012.06.056.

[63] L. Esposito, A. Salem, A. Tucci, A. Gualtieri, S.H. Jazayeri, The use of nepheline-syenite in a body mix for porcelain stoneware tiles, Ceram. Int. 31 (2005) 233–240, https://doi.org/10.1016/j.ceramint.2004.05.006.
[64] M.N. Freire, S.J.G. Sousa, J.N.F. Holanda, Using eggshell waste in red wall tiles, Proc. Inst. Civ. Eng. - Waste Resour. Manag. 161 (2008) 23–27, https://doi.org/10.1680/warm.2008.161.1.23.
[65] B.J. Chow, T. Chen, Y. Zhong, Y. Qiao, Direct formation of structural components using a martian soil simulant, Sci. Rep. 7 (2017) 317, https://doi.org/10.1038/s41598-017-01157-w.
[66] G. Cesaretti, E. Dini, X. de Kestelier, V. Colla, L. Pambaguian, Building components for an outpost on the Lunar soil by means of a novel 3D printing technology, Acta Astronaut. 93 (2014) 430–450, https://doi.org/10.1016/j.actaastro.2013.07.034.
[67] S. Sen, S. Carranza, S. Pillay, Multifunctional Martian habitat composite material synthesized from in situ resources, Adv. Space Res. 46 (2010) 582–592, https://doi.org/10.1016/j.asr.2010.04.009.
[68] A. Alexiadis, F. Alberini, M.E. Meyer, Geopolymers from lunar and Martian soil simulants, Adv. Space Res. 59 (2017) 490–495, https://doi.org/10.1016/j.asr.2016.10.003.
[69] L. Wan, R. Wendner, G. Cusatis, A novel material for in situ construction on Mars: experiments and numerical simulations, Construct. Build. Mater. 120 (2016) 222–231, https://doi.org/10.1016/j.conbuildmat.2016.05.046.
[70] M.R. Smith, J.L. Bandfield, Geology of quartz and hydrated silica-bearing deposits near Antoniadi Crater, Mars, J. Geophys. Res. 117 (2012), https://doi.org/10.1029/2011JE004038.